iScience

CellPress
OPEN ACCESS

Article

Transient titin-dependent ventricular defects during development lead to adult atrial arrhythmia and impaired contractility

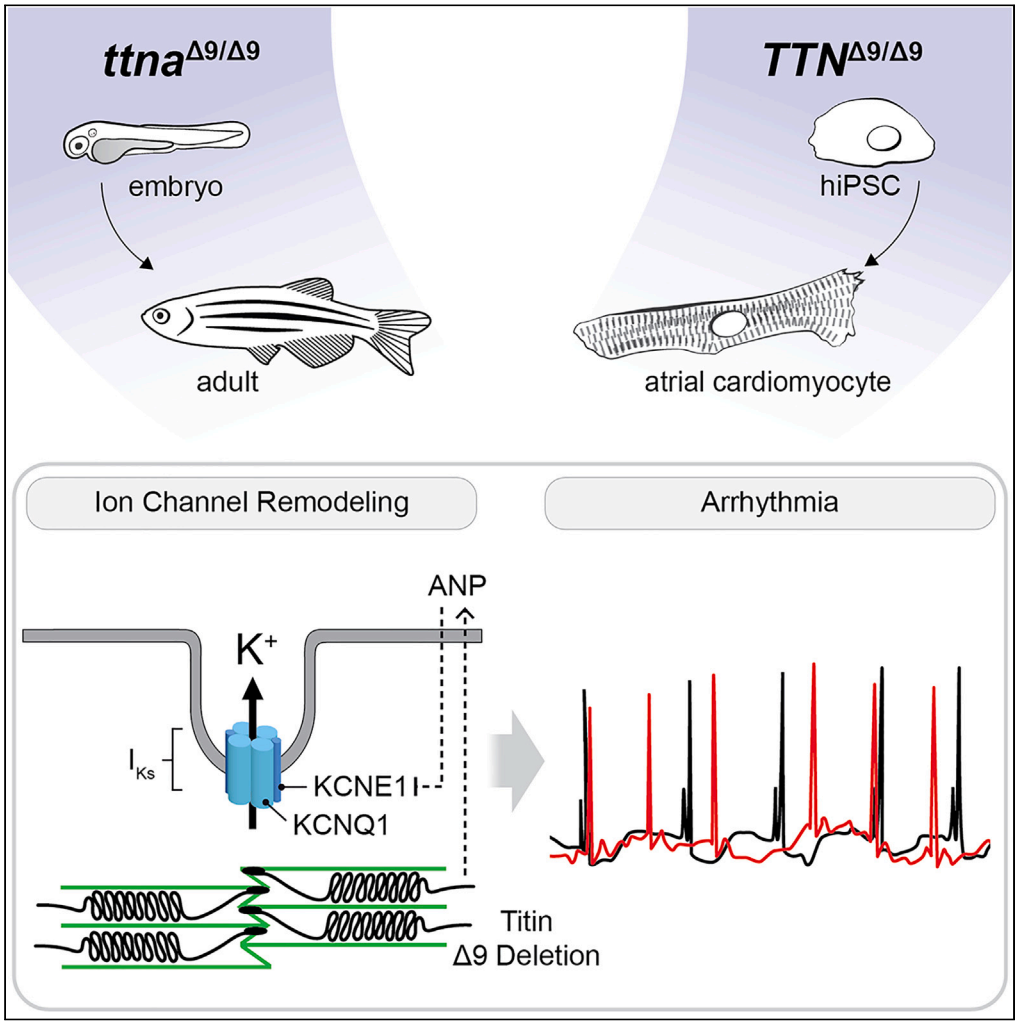

Xinghang Jiang, Olivia T. Ly, Hanna Chen, ..., Yu Gao, Dawood Darbar, Ankur Saxena

darbar@uic.edu (D.D.)
asaxena1@uab.edu (A.S.)

Highlights

A 9-amino acid internal deletion was generated in the titin A-band (*ttna*$^{\Delta 9}$/*TTN*$^{\Delta 9}$)

ttna$^{\Delta 9/\Delta 9}$ zebrafish exhibit developmental defects followed by atrial fibrillation

Aberrant ANP-regulated I_{Ks} remodeling contributes to cardiac defects in mutants

Pharmacological blockade of I_{Ks} rescues arrhythmia and improves atrial contraction

Jiang et al., iScience 27, 110395
July 19, 2024
https://doi.org/10.1016/j.isci.2024.110395

iScience

CellPress
OPEN ACCESS

Article

Transient titin-dependent ventricular defects during development lead to adult atrial arrhythmia and impaired contractility

Xinghang Jiang,[1,2,3,12] Olivia T. Ly,[4,5,12] Hanna Chen,[4] Ziwei Zhang,[6] Beatriz A. Ibarra,[2,3] Mahmud A. Pavel,[4] Grace E. Brown,[5] Arvind Sridhar,[4,7] David Tofovic,[4,8] Abigail Swick,[2,3] Richard Marszalek,[7] Carlos G. Vanoye,[9] Fritz Navales,[2,3] Alfred L. George, Jr.,[9] Salman R. Khetani,[5] Jalees Rehman,[4,10] Yu Gao,[6] Dawood Darbar,[4,8,*] and Ankur Saxena[1,2,3,11,13,*]

SUMMARY

Developmental causes of the most common arrhythmia, atrial fibrillation (AF), are poorly defined, with compensation potentially masking arrhythmic risk. Here, we delete 9 amino acids (Δ9) within a conserved domain of the giant protein titin's A-band in zebrafish and human-induced pluripotent stem cell-derived atrial cardiomyocytes (hiPSC-aCMs). We find that *ttna*$^{\Delta 9/\Delta 9}$ zebrafish embryos' cardiac morphology is perturbed and accompanied by reduced functional output, but ventricular function recovers within days. Despite normal ventricular function, *ttna*$^{\Delta 9/\Delta 9}$ adults exhibit AF and atrial myopathy, which are recapitulated in *TTN*$^{\Delta 9/\Delta 9}$-hiPSC-aCMs. Additionally, action potential is shortened and slow delayed rectifier potassium current (I_{Ks}) is increased due to aberrant atrial natriuretic peptide (ANP) levels. Strikingly, suppression of I_{Ks} in both models prevents AF and improves atrial contractility. Thus, a small internal deletion in titin causes developmental abnormalities that increase the risk of AF via ion channel remodeling, with implications for patients who harbor disease-causing variants in sarcomeric proteins.

INTRODUCTION

Atrial fibrillation (AF), the irregular beating of atria, is the most common type of cardiac arrhythmia and affects millions of adults who are at increased risk of heart failure, stroke, and death.[1–3] Genetic studies have identified more than 140 common genetic loci associated with AF,[4,5] and family-based studies have implicated rare variants primarily encoding cardiac ion channels.[6] However, the advent of high-throughput next-generation sequencing has identified familial/early-onset AF-associated mutations in myocardial structural proteins such as myosin heavy chain 6 (MYH6),[7] myosin light chain 4 (MYL4),[8,9] and, more recently, titin.[10,11] Titin is a major component of the sarcomere and critical for both cardiac development and function.[12] Several titin loss-of-function (LOF) variants are associated with AF,[10,13–16] and both truncating variants (*TTN*tvs) and missense variants can cause dilated cardiomyopathy.[16–21] However, large truncations of titin do not provide mechanistic insight into individual protein domains, especially titin's understudied, highly conserved A-band, which includes 44 immunoglobulin (Ig)-like domains that are enriched in AF-associated variants.[10,13,14,22] Previous work deleting titin's whole I-band/A-band junction uncovered an important role for titin in diastolic dysfunction and heart failure with preserved ejection fraction.[23] However, except for a few Ig-like domains bound to myosin binding protein-C (MBPC),[24] the roles of titin A-band's Ig-like domains are poorly understood.

In some cases, AF correlates with dysregulated cardiac development, which can yield mistakes that increase the risk of adult disease. Congenital heart defects are found in at least 1% of all live births,[25] and individuals with developmental defects are at higher risk for developing AF later in life.[26,27] While there has been rapid progress in uncovering the genetic determinants of abnormal cardiac development, causal genetic relationships between developmental defects and AF are less well-defined.[6,28] It remains unclear if and how adult cardiac

[1]Department of Cell, Developmental, and Integrative Biology, UAB Heersink School of Medicine, Birmingham, AL 35233, USA
[2]Department of Biological Sciences, University of Illinois Chicago, Chicago, IL 60607, USA
[3]University of Illinois Cancer Center, Chicago, IL 60612, USA
[4]Division of Cardiology, Department of Medicine, University of Illinois Chicago, Chicago, IL 60612, USA
[5]Department of Biomedical Engineering, University of Illinois Chicago, Chicago, IL 60607, USA
[6]Department of Pharmaceutical Sciences, University of Illinois Chicago, Chicago, IL 60612, USA
[7]Department of Physiology, University of Illinois Chicago, Chicago, IL 60612, USA
[8]Department of Medicine, Jesse Brown Veterans Administration, Chicago, IL 60612, USA
[9]Department of Pharmacology, Northwestern University, Chicago, IL 60611, USA
[10]Department of Biochemistry and Molecular Genetics, University of Illinois Chicago, Chicago, IL 60607, USA
[11]O'Neal Comprehensive Cancer Center, Birmingham, AL 35233, USA
[12]These authors contributed equally
[13]Lead contact
*Correspondence: darbar@uic.edu (D.D.), asaxena1@uab.edu (A.S.)
https://doi.org/10.1016/j.isci.2024.110395

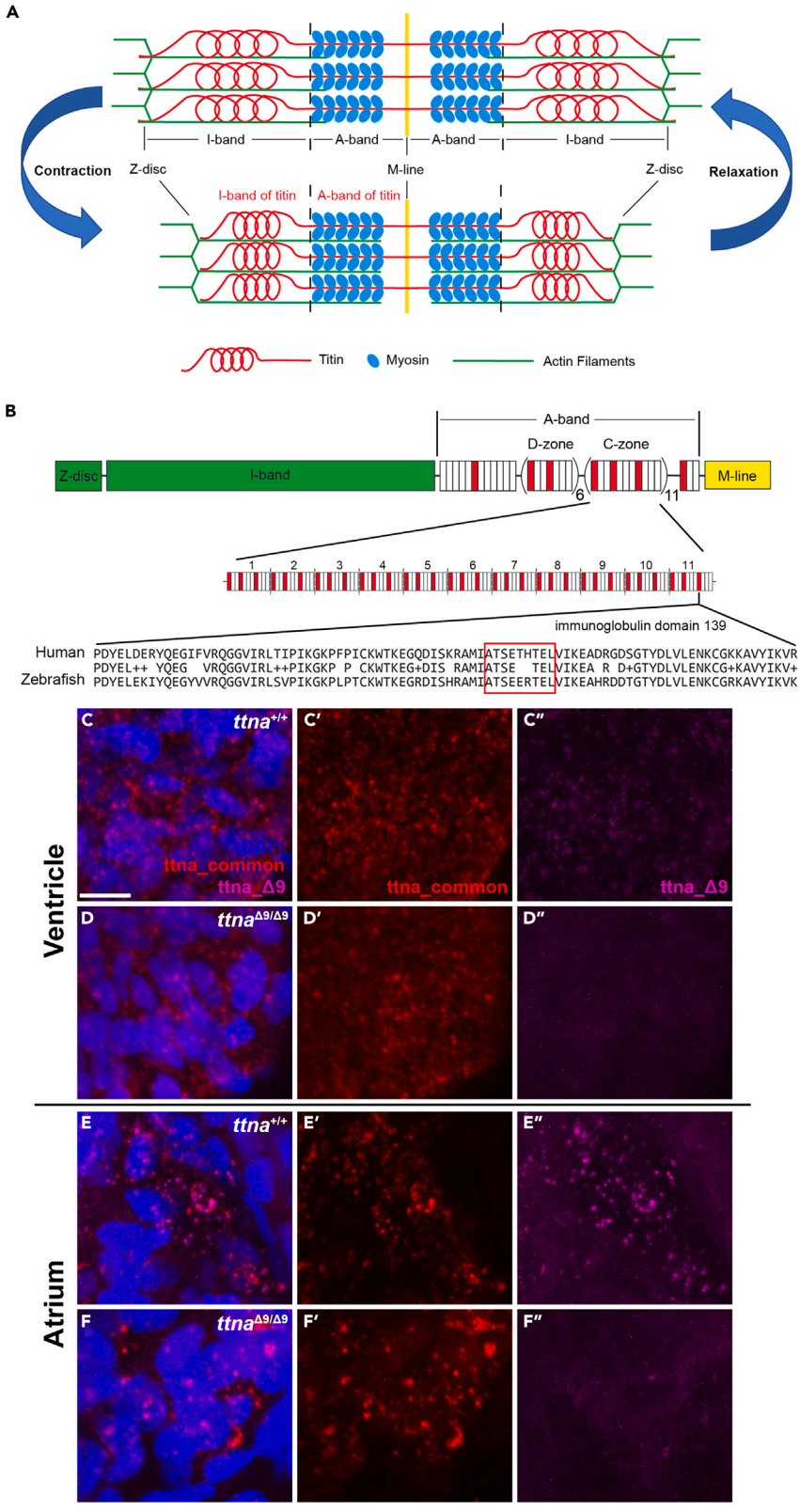
A
I-band
A-band
A-band
I-band
Contraction
Z-disc
M-line
Z-disc
Relaxation
I-band of titin
A-band of titin
Titin
Myosin
Actin Filaments
B
A-band
D-zone
C-zone
Z-disc
I-band
M-line
6
11
1 2 3 4 5 6 7 8 9 10 11
immunoglobulin domain 139
Human PDYELDERYQEGIFVRQGGVIRLTIPIKGKPFPICKWTKEGQDISKRAMIATSETHTELVIKEADRGDSGTYDLVLENKCGKKAVYIKVR
PDYEL++ YQEG VRQGGVIRL++PIKGKP P CKWTKEG+DIS RAMIATSE TELVIKEA R D+GTYDLVLENKCG+KAVYIKV+
Zebrafish PDYELEKIYQEGYVVRQGGVIRLSVPIKGKPLPTCKWTKEGRDISHRAMIATSEERTELVIKEAHRDDTGTYDLVLENKCGRKAVYIKVK
C ttna+/+
C′
C″
DAPI
ttna_common
ttna_Δ9
ttna_common
ttna_Δ9
Ventricle
D ttnaΔ9/Δ9
D′
D″
E ttna+/+
E′
E″
Atrium
F ttnaΔ9/Δ9
F′
F″

Figure 1. *ttna*$^{\Delta 9}$ results in a 9 amino acid deletion in an immunoglobin-like domain corresponding to the human Ig-139 domain of titin A-band

(A) Schematic of major components of the sarcomere.

(B) Schematic of the full-length human titin protein and detailed layout of the C-zone in the A-band. Red, Ig domain. White, fibronectin type-III (FN3) domain. There are 11 repeats of Ig-FN3-FN3-Ig-FN3-FN3-FN3-Ig-FN3-FN3-FN3 pattern of domains in the C-zone. Amino acid sequence alignment between human Ig domain 139 (Ig-139) and its corresponding Ig domain (Ig-107) in the zebrafish ttna protein. Red box indicates the location of residues deleted in the *TTN* $^{\Delta 9}$ and *ttna*$^{\Delta 9}$ mutation.

(C–F″) Representative 3D projection images of *in situ* hybridization chain reaction with probes targeting *ttna* mRNA in either the 27 base pair deleted region (ttna_Δ9, magenta) or regions approximately 1,500 base pairs upstream and downstream of the deletion (ttna_common, red) in ventricular (C–D″) and atrial (E–F″) cardiomyocytes of wild-type (*ttna*$^{+/+}$, $n = 6$) and *ttna*$^{\Delta 9/\Delta 9}$ ($n = 6$) zebrafish embryos at 48 h postfertilization (hpf). Optical section thickness: 29.8 μm. Scale bar: 10 μm. See also Figure S1.

function can adapt to undiagnosed and/or transient developmental defects and if compensatory recovery might mask an increased risk for AF in adulthood. Meanwhile, genetic studies have revealed a crucial role for ion channel remodeling in AF pathogenesis, but potential non-canonical roles for structural proteins in regulating atrial arrhythmogenicity are poorly understood.

A potential connection between titin's roles in cardiac development and adult functionality has not been explored. Postulating that a small alteration in titin, with its canonical structural role in the sarcomere, may give rise to unexpected lasting effects in adults, we deleted just 9 amino acids (Δ9) within an A-band Ig-like domain in both *TTN*'s zebrafish orthologue *ttna* and in *TTN* itself in human-induced pluripotent stem cell-derived atrial cardiomyocytes (hiPSC-aCMs).[29,30] Upon interrogating titin's role in both cardiac development and function, including AF pathogenesis, we find that homozygous mutant *ttna*$^{\Delta 9/\Delta 9}$ embryos demonstrate defects in atrial morphology and contraction as well as overall cardiac function in comparison to *ttna*$^{+/+}$ clutchmates. Most *ttna*$^{\Delta 9/\Delta 9}$ embryos survive these initial defects and exhibit significant improvement in ventricular function by 72–96 h post fertilization (hpf), with 78% of homozygous embryos surviving to adulthood. However, *ttna*$^{\Delta 9/\Delta 9}$ adult zebrafish and mature *TTN*$^{\Delta 9/\Delta 9}$-hiPSC-aCMs exhibit AF, atrial cardiomyopathy without fibrosis, sarcomeric disassembly, reduced contraction, and atrial action potential (AP) shortening. We also identify aberrant atrial natriuretic peptide (ANP) expression leading to enhanced slow delayed rectifier potassium current (I_{Ks}). Finally, targeted pharmacological inhibition of I_{Ks} both *in vivo* and *in vitro* ameliorates Δ9-driven AF and improves atrial contractility. Collectively, these data reveal a progression from developmental defects to functional recovery to I_{Ks}-dependent AF due to *TTN*$^{\Delta 9}$-dependent ion channel remodeling and atrial cardiomyopathy, suggesting that ion channel modulation may offer a new therapeutic strategy for improving cardiac function in patients with mutations in structural proteins.

RESULTS

Targeted *ttna* mutagenesis yields a 9-amino acid deletion within zebrafish titin's Ig-107 domain

To investigate the role of titin's A-band in cardiac development and disease, we performed targeted CRISPR-Cas9-mediated mutagenesis of *TTN*'s zebrafish orthologue, *ttna*, which is the dominant orthologue required for zebrafish embryo cardiac sarcomere assembly and contraction.[31] The resulting *ttna*$^{\Delta 9}$ allele harbors a 9-amino acid, in-frame deletion (Chromosome 9: 42905440–42905466, GRCz11; p.Ala29817_Leu29825del, UniProt ID: A5X6X5) within the A-band in the Ig-107 domain, which corresponds to human *TTN*'s Ig-139 domain (UniProt ID: Q8WZ42) (Figures 1A and 1B). *In situ* hybridization chain reaction (HCR)[13] in zebrafish embryos targeted *ttna* mRNA's 27 base pair deleted region or regions ∼1.5 kb upstream and downstream of the deletion. Probes targeting the flanking regions detected similar levels of *ttna* mRNA in wild-type (WT) *ttna*$^{+/+}$ and homozygous mutant *ttna*$^{\Delta 9/\Delta 9}$ cardiomyocytes (Figures 1C–1D′ and 1E–1F′), while the deleted region was detected only in *ttna*$^{+/+}$ cardiomyocytes (Figures 1C″, 1D″, 1E″, and 1F″), confirming the deletion and unperturbed transcription of *ttna*$^{\Delta 9}$ mRNA. Similar results were observed in skeletal muscle tissue (Figure S1), consistent with the known conservation of A-band Ig domains across almost all titin isoforms and their expression in striated muscles.[32,33]

ttna$^{\Delta 9/\Delta 9}$ zebrafish exhibit a transient reduction in ventricular function during development

ttna, the first sarcomeric gene expressed in the zebrafish heart, is essential for sarcomere assembly and cardiac contractility.[31] Therefore, we employed transmission electron microscopy (TEM) to determine the sarcomeric organization of embryonic cardiomyocytes at 48 hpf, when significant assembly of the sarcomere has already occurred.[34] We found that *ttna*$^{+/+}$ and *ttna*$^{\Delta 9/\Delta 9}$ embryonic cardiomyocytes exhibit similar organization and sarcomere length (Figures 2A, 2B, and S2A), indicating that *ttna*$^{\Delta 9}$ does not disrupt sarcomere assembly during cardiac development.

To determine organ-level functionality, we examined cardiac chamber morphology and function in live embryos by crossing *ttna*$^{\Delta 9/+}$ zebrafish into the background of cmlc2:eGFP; gata1:dsRed transgenic zebrafish, labeling cardiomyocytes and red blood cells. Almost all (91%) *ttna*$^{\Delta 9/\Delta 9}$ embryos exhibit successful heart looping, but once atria and ventricles are well-formed at 48 hpf, *ttna*$^{\Delta 9/\Delta 9}$;eGFP+; dsRed+ (hereafter termed *ttna*$^{\Delta 9/\Delta 9}$) embryos have slightly smaller ventricles (Figures 2C and S2B), reduced ventricular contraction (Figures 2D and S2C), and slower blood circulation (Figure 2E; Video S1) in comparison to *ttna*$^{+/+}$;eGFP+; dsRed+ and *ttna*$^{\Delta 9/+}$;eGFP+; dsRed+ (hereafter termed *ttna*$^{+/+}$ and *ttna*$^{\Delta 9/+}$) clutchmates. However, ventricular size, contraction, and blood circulation recover in *ttna*$^{\Delta 9/\Delta 9}$ embryos to a similar level as that observed in clutchmates by 72 hpf and 96 hpf (Figures 2C–2E and S2C; Video S1). Consistent with these measurements, blood regurgitation and pooling in the inflow tract at 48 hpf also improve by 72–96 hpf (Figures 2F–2K; Video S2). Meanwhile, heart rate and rhythm are unchanged throughout these time points (48–96 hpf; Figures S2D and S2E). Approximately 78% of *ttna*$^{\Delta 9/\Delta 9}$ embryos grow to be active and fertile adults, compared to *ttna*$^{\Delta 9/+}$ and *ttna*$^{\Delta 9/\Delta 9}$ clutchmates. Having observed no *ttna*$^{\Delta 9/+}$ phenotypes, we analyzed *ttna*$^{\Delta 9/\Delta 9}$ adults alongside *ttna*$^{+/+}$ clutchmates and found ventricles of a similar size (Figure 2L) as well as a similarly organized but slightly elongated sarcomere

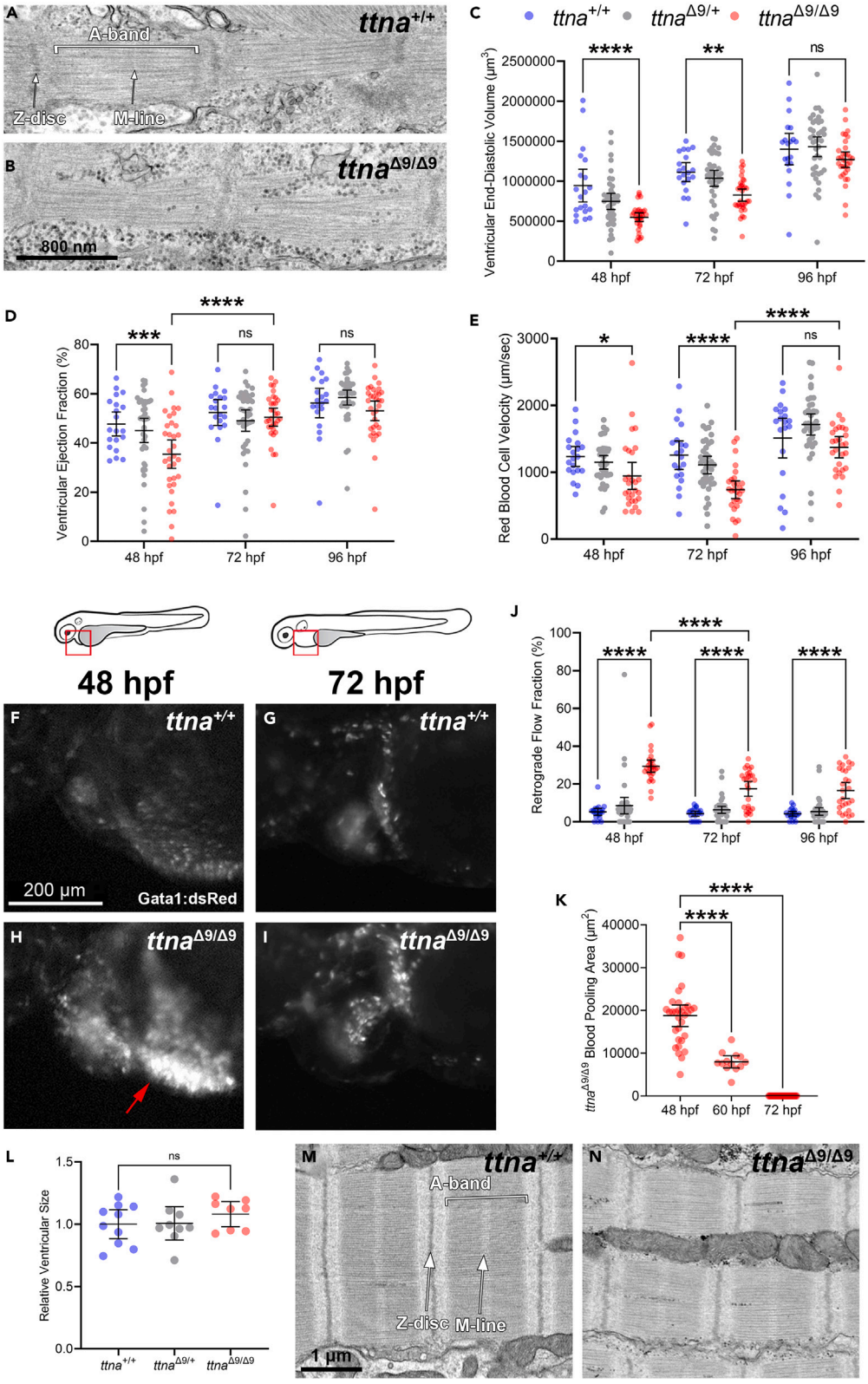
A
A-band
Z-disc
M-line
ttna+/+
B
ttnaΔ9/Δ9
800 nm
C
ttna+/+
ttnaΔ9/+
ttnaΔ9/Δ9
Ventricular End-Diastolic Volume (µm3)
2500000
2000000
1500000
1000000
500000
0
****
**
ns
48 hpf
72 hpf
96 hpf
D
Ventricular Ejection Fraction (%)
80
60
40
20
0
****
***
ns
ns
48 hpf
72 hpf
96 hpf
E
Red Blood Cell Velocity (µm/sec)
3000
2000
1000
0
*
****
****
ns
48 hpf
72 hpf
96 hpf
48 hpf
72 hpf
F
ttna+/+
200 µm
Gata1:dsRed
G
ttna+/+
H
ttnaΔ9/Δ9
I
ttnaΔ9/Δ9
J
Retrograde Flow Fraction (%)
100
80
60
40
20
0
****
****
****
****
48 hpf
72 hpf
96 hpf
K
ttnaΔ9/Δ9 Blood Pooling Area (µm2)
40000
30000
20000
10000
0
****
****
48 hpf
60 hpf
72 hpf
L
Relative Ventricular Size
1.5
1.0
0.5
0.0
ns
ttna+/+
ttnaΔ9/+
ttnaΔ9/Δ9
M
ttna+/+
A-band
Z-disc
M-line
1 µm
N
ttnaΔ9/Δ9

Figure 2. *ttna*$^{\Delta 9/\Delta 9}$ zebrafish exhibit a transient reduction in ventricular function during development

(A and B) Representative transmission electron microscopy (TEM) images of sarcomeres in wild-type (*ttna*$^{+/+}$, $n = 2$) and *ttna*$^{\Delta 9/\Delta 9}$ ($n = 5$) zebrafish embryonic cardiomyocytes at 48 hpf.

(C–E) Quantification of ventricular end-diastolic volume (C), ejection fraction (D), and red blood cell velocity (E) for *ttna*$^{+/+}$, *ttna*$^{\Delta 9/+}$, and *ttna*$^{\Delta 9/\Delta 9}$ embryos at 48, 72, and 96 hpf.

(F–I) Representative images of wild-type and *ttna*$^{\Delta 9/\Delta 9}$ embryos' blood flow in the inflow tract, visualized with the red blood cell-labeling transgenic line gata1:dsRed at 48 and 72 hpf. Red boxes indicate the location of the inflow tract, and red arrow indicates blood pooling.

(J) Quantification of the blood retrograde flow fraction between the atrium and inflow tract for *ttna*$^{+/+}$, *ttna*$^{\Delta 9/+}$, and *ttna*$^{\Delta 9/\Delta 9}$ embryos at 48, 72, and 96 hpf.

(K) Quantification of blood-pooling area in the inflow tract of *ttna*$^{\Delta 9/\Delta 9}$ embryos at 48, 60, and 72 hpf.

(L) 12–15-months-old *ttna*$^{+/+}$ ($n = 10$), *ttna*$^{\Delta 9/+}$ ($n = 9$), and *ttna*$^{\Delta 9/\Delta 9}$ ($n = 8$) ventricular relative size.

(M and N) Representative TEM images of sarcomeres in *ttna*$^{+/+}$ ($n = 3$) and *ttna*$^{\Delta 9/\Delta 9}$ ($n = 3$) ventricular cardiomyocytes at 6 months of age. *n* value for (C–K): *ttna*$^{+/+}$ $n = 20$, *ttna*$^{\Delta 9/+}$ $n = 39$, *ttna*$^{\Delta 9/\Delta 9}$ $n = 33$. Data in (C–E, J–L) are represented as mean ±95% confidence intervals. ns $p > 0.05$; *$p < 0.05$; **$p < 0.01$; ***$p < 0.001$; ****$p < 0.0001$. See also Figures S2 and S4.

structure (Figures 2M–2N and S2F). Collectively, these data indicate that *ttna*$^{\Delta 9/\Delta 9}$ embryos have initial physiological and functional defects that rapidly recover, providing sufficient ventricular function and normal electrophysiology for survival and growth.

ttna$^{\Delta 9/\Delta 9}$ zebrafish exhibit persistent atrial enlargement, and sarcomeric disorganization is present in both adult *ttna*$^{\Delta 9/\Delta 9}$ zebrafish atrial cardiomyocytes and *TTN*$^{\Delta 9/\Delta 9}$-hiPSC-aCMs

In contrast to their ventricular recovery, *ttna*$^{\Delta 9/\Delta 9}$ embryos develop and sustain significant atrial enlargement in comparison to *ttna*$^{+/+}$ and *ttna*$^{\Delta 9/+}$ clutchmates from 48 to 96 hpf (Figures 3A–3C and S3A; Video S3), suggesting a primary atrial phenotype. At 96 hpf, *ttna*$^{\Delta 9/\Delta 9}$ embryos exhibit an abnormally bulbous atrial shape (Figures 3A, 3B, and S3B) and significantly thickened atrial walls (Figures 3D–3F), while *ttna*$^{\Delta 9/\Delta 9}$ ventricular morphology and thickness are normal (Figures S3C–S3E). Atrial enlargement persists in *ttna*$^{\Delta 9/\Delta 9}$ adults (Figures 3G–3I) and lacks atrial fibrosis (Figures 3J and 3K), consistent with unchanged levels of titin and the profibrotic proteins col1a1b and acta2 (Figure S4A). Additionally, *ttna*$^{\Delta 9/\Delta 9}$ adult zebrafish atrial cardiomyocytes have significantly disorganized and shortened sarcomeres, including M-line absence and blurry boundaries between light and dark bands, in comparison to both *ttna*$^{+/+}$ atrial cardiomyocytes and *ttna*$^{\Delta 9/\Delta 9}$ ventricular cardiomyocytes (Figures 2N, 3L, 3M, and S4B), indicating an atrial-specific phenotype that persists in adults.

To determine the Δ9 deletion's effects in human cardiomyocytes, we generated *TTN*$^{\Delta 9}$ mutant hiPSCs and applied electrometabolic maturation (EMM) for the generation of mature hiPSC-aCMs.[35] Retinoic acid (RA) was used to induce aCM differentiation from hiPSCs. Flow cytometry revealed a significant increase in the percentage of cells expressing Kv1.5 in RA-treated cells compared to dimethyl sulfoxide (DMSO)-treated cells in both *TTN*$^{+/+}$-hiPSC-aCMs and *TTN*$^{\Delta 9/\Delta 9}$-hiPSC-aCMs (Figure S5). We also applied cardiac micropatterning and coculture (cMPCC) with atrial fibroblasts to create a comprehensive EMM-cMPCC protocol (Figure S6).[36] Clearly demarcated Z-discs and M-lines are visible in *TTN*$^{+/+}$-hiPSC-aCMs (Figures 3N and 3N'), whereas *TTN*$^{\Delta 9/\Delta 9}$-hiPSC-aCM organization is diffuse and lacks consistent Z and M-lines (Figures 3O and 3O'). *TTN*$^{\Delta 9/\Delta 9}$-hiPSC-aCMs demonstrate decreased sarcomeric organization and significantly shortened sarcomere lengths (Figures 3P–3T).

ttna$^{\Delta 9/\Delta 9}$ zebrafish atria and *TTN*$^{\Delta 9/\Delta 9}$-hiPSC-aCMs both exhibit reduced contraction, and *ttna*$^{\Delta 9/\Delta 9}$ adult zebrafish exhibit AF

Consistent with their developmental morphological defects, *ttna*$^{\Delta 9/\Delta 9}$ embryos have reduced atrial contraction in comparison to *ttna*$^{+/+}$ and *ttna*$^{\Delta 9/+}$ clutchmates (Figure 4A; Video S3). To determine the persistence of this functional change, we performed transthoracic echocardiography and Doppler pulse wave imaging and found that *ttna*$^{\Delta 9/\Delta 9}$ and *ttna*$^{\Delta 9/+}$ adults exhibit reduced peak A wave velocities, with no change in peak E wave velocities (Figure S7; Table S1). These results indicate persistent reduction in atrial contraction and atrial-dependent ventricular filling in *ttna*$^{\Delta 9/\Delta 9}$ adults, while potential long-lasting effects of the *ttna*$^{\Delta 9/+}$ heterozygous mutation decrease atrial contraction in *ttna*$^{\Delta 9/+}$ adults. Similarly, *TTN*$^{\Delta 9/\Delta 9}$-hiPSC-aCMs demonstrate significant defects in both contraction and relaxation (Figures 4B and 4C; Videos S4 and S5). Compared to *TTN*$^{+/+}$-hiPSC-aCMs, *TTN*$^{\Delta 9/\Delta 9}$-hiPSC-aCMs display increased contraction frequency (Figure 4D), reduced displacement (a surrogate marker of relative force) (Figure 4E), shortened wave duration (Figure 4F), and decreased maximum velocity (Figure 4G).

To investigate whether the observed structural and functional changes might lead to electrophysiological abnormalities, we performed electrocardiography and found that 52% of *ttna*$^{\Delta 9/\Delta 9}$ adult zebrafish demonstrate P-wave loss and irregular R-R intervals, indicating AF (Figures 5A–5C). To test whether cellular electrophysiology is affected by the Δ9 deletion, we performed *ex vivo* patch-clamp and optical voltage mapping experiments on adult zebrafish *ttna*$^{\Delta 9/\Delta 9}$ atrial cardiomyocytes and *TTN*$^{\Delta 9/\Delta 9}$-hiPSC-aCMs, respectively, and observed altered AP amplitudes (APAs) and shortened AP durations (APDs) in both model systems (Figures 5D–5G and S8).

ttna$^{\Delta 9/\Delta 9}$ zebrafish embryos and *TTN*$^{\Delta 9/\Delta 9}$-hiPSC-aCMs exhibit aberrant ANP regulation and ANP-dependent changes in I_{Ks}

We next explored how our transient ventricular and persistent atrial embryonic defects could mechanistically lead to adult AF. The ANP hormone has been shown to be overexpressed in response to ventricular dysfunction by reactivation of developmental gene expression,[37–39] and its overexpression has been linked to AF via an increased slow delayed rectifier potassium current (I_{Ks}).[30,40] The I_{Ks} channel in cardiomyocytes consists of KCNQ1 and KCNE1 subunits, with KCNQ1 functioning as the pore-forming subunit and KCNE1 as a regulator subunit.[41–43] We first examined mRNA expression levels for ANP (*nppa*), *kcnq1*, and *kcne1* in zebrafish embryos and found that, at 48 hpf, *nppa* expression is

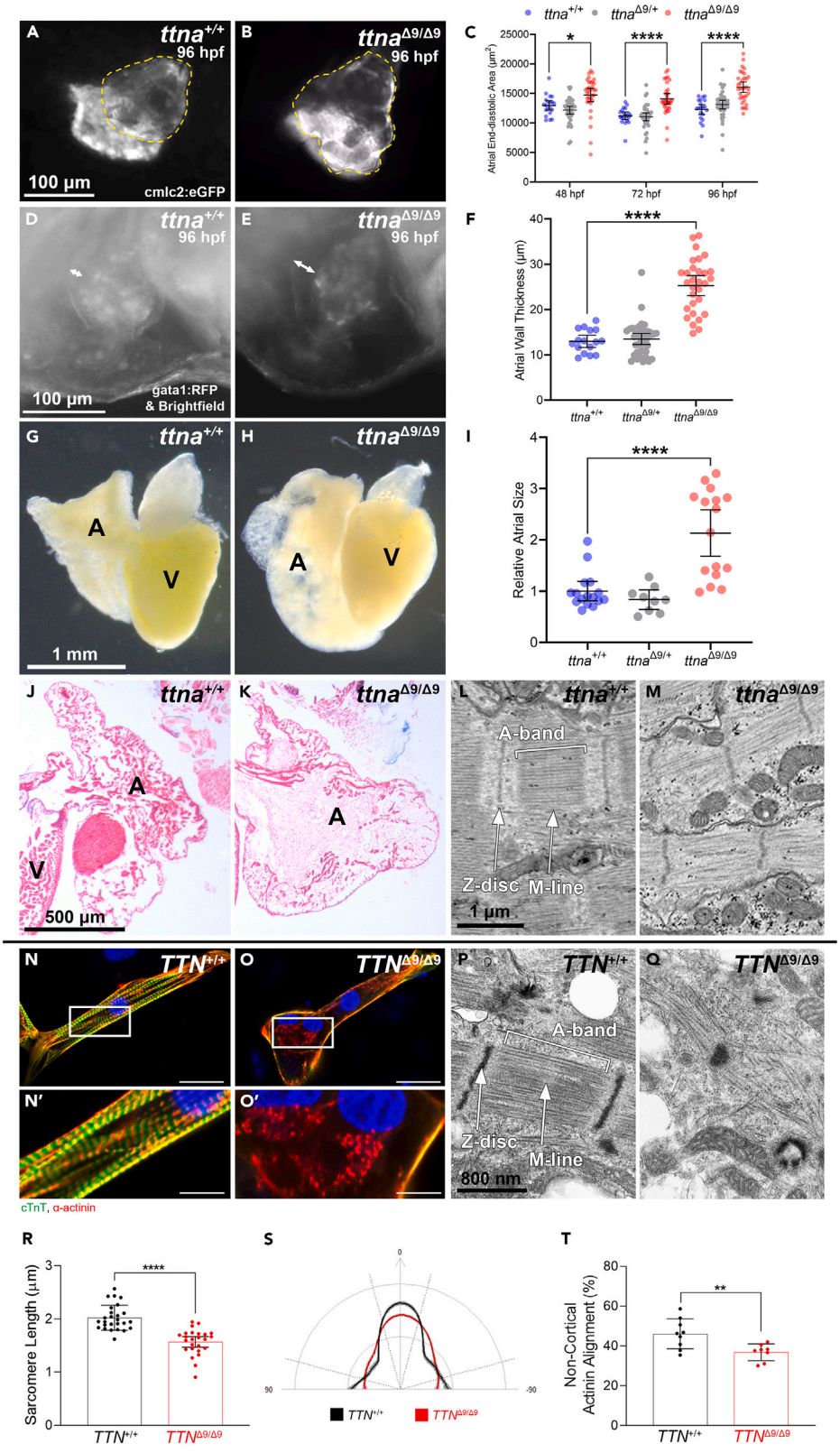
A
ttna+/+
96 hpf
100 μm
cmlc2:eGFP
B
ttnaΔ9/Δ9
96 hpf
C
ttna+/+
ttnaΔ9/+
ttnaΔ9/Δ9
Atrial End-diastolic Area (μm2)
25000
20000
15000
10000
5000
0
*
****
****
48 hpf
72 hpf
96 hpf
D
ttna+/+
96 hpf
100 μm
gata1:RFP
& Brightfield
E
ttnaΔ9/Δ9
96 hpf
F
Atrial Wall Thickness (μm)
40
30
20
10
0
****
ttna+/+
ttnaΔ9/+
ttnaΔ9/Δ9
G
ttna+/+
A
V
1 mm
H
ttnaΔ9/Δ9
A
V
I
Relative Atrial Size
4
3
2
1
0
****
ttna+/+
ttnaΔ9/+
ttnaΔ9/Δ9
J
ttna+/+
A
V
500 μm
K
ttnaΔ9/Δ9
A
L
ttna+/+
A-band
Z-disc
M-line
1 μm
M
ttnaΔ9/Δ9
N
TTN+/+
N′
O
TTNΔ9/Δ9
O′
cTnT, α-actinin
P
TTN+/+
A-band
Z-disc
M-line
800 nm
Q
TTNΔ9/Δ9
R
Sarcomere Length (μm)
3
2
1
0
****
TTN+/+
TTNΔ9/Δ9
S
0
90
-90
TTN+/+
TTNΔ9/Δ9
T
Non-Cortical Actinin Alignment (%)
80
60
40
20
0
**
TTN+/+
TTNΔ9/Δ9

Figure 3. *ttna*$^{\Delta9/\Delta9}$ zebrafish exhibit persistent atrial enlargement, and sarcomeric disorganization is found in *ttna*$^{\Delta9/\Delta9}$ zebrafish atrial cardiomyocytes and *TTN*$^{\Delta9/\Delta9}$-hiPSC-aCMs

(A and B) Representative images of 96 hpf *ttna*$^{+/+}$ and *ttna*$^{\Delta9/\Delta9}$ zebrafish hearts visualized with the cardiomyocyte-labeling transgenic line cmlc2:eGFP. Yellow dashed lines outline the atria.

(C) Quantification of atrial end-diastolic area for *ttna*$^{+/+}$ (n = 20), *ttna*$^{\Delta9/+}$ (n = 39), and *ttna*$^{\Delta9/\Delta9}$ (n = 33) embryos at 48, 72, and 96 hpf.

(D–F) Representative images of 96 hpf *ttna*$^{+/+}$ and *ttna*$^{\Delta9/\Delta9}$ hearts and blood visualized with bright field and the red blood cell-labeling transgenic line gata1:dsRed, respectively. White arrows indicate the atrial myocardial wall. (F) Quantification of atrial myocardial wall thickness at 96 hpf. n value: *ttna*$^{+/+}$ = 16, *ttna*$^{\Delta9/+}$ = 37, *ttna*$^{\Delta9/\Delta9}$ = 32.

(G and H) Representative bright-field images of dissected hearts from 8–15-months-old *ttna*$^{+/+}$ and *ttna*$^{\Delta9/\Delta9}$ zebrafish. A, atrium. V, ventricle.

(I) Relative atrial size of *ttna*$^{+/+}$ (n = 16), *ttna*$^{\Delta9/\Delta9}$ (n = 9), and *ttna*$^{\Delta9/\Delta9}$ (n = 16) zebrafish.

(J and K) Representative images of atria trichrome staining from 12-months-old *ttna*$^{+/+}$ (n = 4) and *ttna*$^{\Delta9/\Delta9}$ (n = 3) zebrafish. A, atrium. V, ventricle.

(L and M) Representative TEM images of sarcomeres in *ttna*$^{+/+}$ (n = 3) and *ttna*$^{\Delta9/\Delta9}$ (n = 3) zebrafish atrial cardiomyocytes at 6 months of age.

(N–O′) Representative images of immunofluorescence staining targeting cardiac troponin T (cTnT; green) and α-actinin (red) in *TTN*$^{+/+}$-hiPSC-aCMs (N) and *TTN*$^{\Delta9/\Delta9}$-hiPSC-aCMs (O) with insets (N′, O′). Scale bar: (N, O) 30 μm; (N′, O′) 15 μm.

(P and Q) Representative TEM images of *TTN*$^{+/+}$-hiPSC-aCMs and *TTN*$^{\Delta9/\Delta9}$-hiPSC-aCMs.

(R–T) Quantification of sarcomeric length in *TTN*$^{+/+}$-hiPSC-aCMs and *TTN*$^{\Delta9/\Delta9}$-hiPSC-aCMs (n = 3 independent batches, n = 8–9 cells per batch). (S–T) Measurement of non-cortical actinin alignment against perpendicular and parallel axes of *TTN*$^{+/+}$-hiPSC-aCMs and *TTN*$^{\Delta9/\Delta9}$-hiPSC-aCMs (n = 3 independent batches, n = 2–3 cells per batch). Data in (C, F, I, R, and T) are represented as mean ±95% confidence intervals. *p < 0.05; **p < 0.01; ****p < 0.0001. See also Figures S3–S6.

significantly higher, *kcnq1* is unchanged, and *kcne1* is significantly lower in *ttna*$^{\Delta9/\Delta9}$ embryos in comparison with *ttna*$^{+/+}$ clutchmates (Figure 6A), with ANP overexpression persisting in adult *ttna*$^{\Delta9/\Delta9}$ atria (Figure S4A). To establish a direct connection between ANP and the downregulation of *kcne1*/*KCNE1* in the Δ9 deletion, we injected a translation-blocking morpholino targeting ANP in both *ttna*$^{+/+}$ and *ttna*$^{\Delta9/\Delta9}$ zebrafish embryos. ANP knockdown in *ttna*$^{\Delta9/\Delta9}$ embryos yields increased *kcne1* expression (Figure 6B) and improved atrial contraction in comparison to control morpholino-treated *ttna*$^{\Delta9/\Delta9}$ embryos (Figure 6C). In contrast, both atrial contraction in *ttna*$^{+/+}$ embryos and ventricular contraction in *ttna*$^{\Delta9/\Delta9}$ zebrafish embryos remain unaffected (Figures 6D and 6E). Finally, knockdown of closely related brain natriuretic peptide (BNP) fails to improve *ttna*$^{\Delta9/\Delta9}$ embryonic atrial contraction (Figure S9), pointing to the specificity of an ANP-mediated effect.

We also examined *NPPA* expression in mature *TTN*$^{\Delta9/\Delta9}$-hiPSC-aCMs and found it to be significantly downregulated (Figure S10A) in contrast to the upregulation observed in *ttna*$^{\Delta9/\Delta9}$ adult zebrafish atria. Meanwhile, we observed greater *KCNQ1* and lower *KCNE1* expression in *TTN*$^{\Delta9/\Delta9}$- versus *TTN*$^{+/+}$-hiPSC-aCMs (Figure S10B). Collectively, our data suggest that Δ9 deletion-induced aberrant regulation of ANP expression impairs atrial function via I_{Ks} channel modulation.

ttna$^{\Delta9/\Delta9}$ zebrafish atrial cardiomyocytes and *TTN*$^{\Delta9/\Delta9}$-hiPSC-aCMs demonstrate I_{Ks} potassium channel remodeling

To determine whether I_{Ks} function is affected by Δ9's downregulation of *KCNE1*, we performed high-throughput whole-cell voltage clamping of hiPSC-aCMs. While sodium (I_{Na}) and L-type calcium current ($I_{Ca,L}$) densities are not different (Figure S11), peak I_{Ks} density is significantly higher in *TTN*$^{\Delta9/\Delta9}$-hiPSC-aCMs in comparison to *TTN*$^{+/+}$-hiPSC-aCMs (Figures 7A and 7B).

Targeted pharmacological blockade of I_{Ks} rescues arrhythmia and improves atrial contraction and relaxation in *TTN*$^{\Delta9/\Delta9}$-hiPSC-aCMs and *ttna*$^{\Delta9/\Delta9}$ zebrafish atria

To further understand the relevance of a Δ9-mediated increase in I_{Ks}, we first treated both *TTN*$^{+/+}$- and *TTN*$^{\Delta9/\Delta9}$-hiPSC-aCMs with vehicle (DMSO) and observed marked APD_{90} shortening and irregular AP impulses in the latter, indicative of AF (Figures 7C–7E). While the addition of the calcium channel blocker verapamil has no effect (Figure S12), the addition of the I_{Ks}-blocker HMR-1556 abrogates APD_{90} shortening and prevents induction of AF (Figures 7C–7E). HMR-1556 treatment also improves atrial contractility of *TTN*$^{\Delta9/\Delta9}$-hiPSC-aCMs, indicated by a similar level of contraction frequency, relaxation, and wave component duration to that seen in *TTN*$^{+/+}$-hiPSC-aCMs (Figures 7F–7J and S13A; Videos S6, S7, and S8), while maximal velocity is unaffected (Figure S13B).

We similarly treated *ttna*$^{\Delta9/\Delta9}$ zebrafish with HMR-1556 at 50–54 hpf and found that, as early as 54 hpf, I_{Ks} inhibition accelerates the recovery of atrial contraction, with contractility comparable to that seen in untreated *ttna*$^{\Delta9/\Delta9}$ embryos 42 h later (96 hpf; Figures 4A, 7K, and S13C; Video S9), while atrial size and wall thickness are unaffected (Figures S13D and S13E). Collectively, these data across both models suggest that a *TTN*$^{\Delta9/\Delta9}$/*ttna*$^{\Delta9/\Delta9}$-mediated increase in I_{Ks} contributes to AF, reduced atrial contraction, and atrial cardiomyopathy.

DISCUSSION

Elucidating the molecular mechanisms by which developmental defects lead to increased risk of AF in adults has been challenging, with rare known examples such as the association of the developmentally important transcription factor paired-like homeodomain transcription factor 2 (*PITX2*) with common forms of AF.[44] Meanwhile, titin contributes to the structural formation and integrity of the developing and adult heart[12], with *TTN*tvs associated not only with AF and dilated cardiomyopathy[10,13–20] but also increased mortality for early-onset AF patients harboring *TTN*tvs.[11] However, the mechanism(s) by which *TTN*tvs cause AF has been elusive, partly due to broad analysis of large truncations that eliminate numerous distinct regions such as the understudied A-band Ig domains, leaving titin's domain-specific functions unclear. Here, to explore the relationship between developmental defects and the pathogenesis of AF, we deleted just 9 amino acids in titin's A-band and

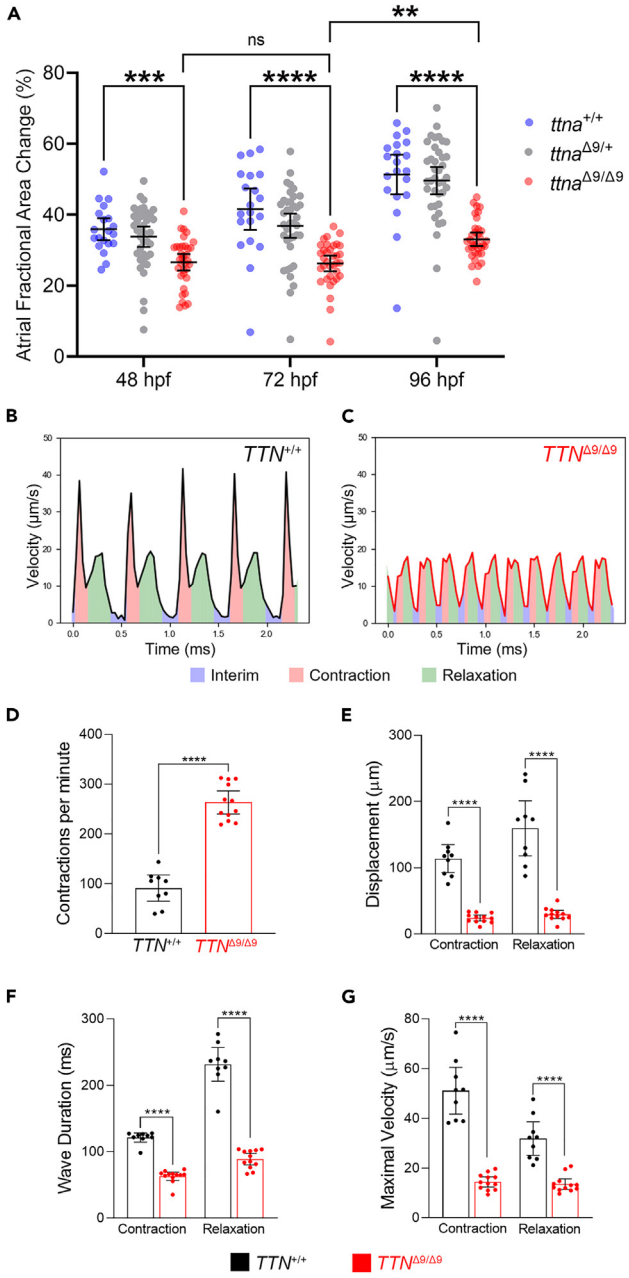

Figure 4. *ttna*$^{\Delta 9/\Delta 9}$ zebrafish atria and *TTN*$^{\Delta 9/\Delta 9}$-hiPSC-aCMs exhibit reduced atrial contractility

(A) Quantification of atrial contraction for *ttna*$^{+/+}$ (n = 20), *ttna*$^{\Delta 9/+}$ (n = 39), and *ttna*$^{\Delta 9/\Delta 9}$ (n = 33) embryos at 48, 72, and 96 hpf.

(B and C) Representative recordings of the contraction of *TTN*$^{+/+}$-hiPSC-aCMs and *TTN*$^{\Delta 9/\Delta 9}$-hiPSC-aCMs.

(D–G) Quantification of contraction frequency (D), displacement (E), wave component duration (F), and maximal velocity (G) during contraction and relaxation of hiPSC-aCMs (n = 3 independent batches, n = 3 biological replicates per batch). Data in (A, D–G) are represented as mean ±95% confidence intervals. ns $p > 0.05$; **$p < 0.01$; ***$p < 0.001$; ****$p < 0.0001$. See also Figure S7 and Table S1.

identified an unexpected role for this giant protein in mediating both ion channel-dependent remodeling and impaired atrial contractility. Notably, early cardiac dysfunction and recovery lead to aberrant ANP expression and ion channel remodeling, with potential implications for how subtle structural mutations might cause subclinical abnormalities that lead to AF in adulthood.

Previous studies have revealed an association between *TTN*tvs and early-onset AF,[16] but the underlying mechanisms are poorly understood. Additionally, heterozygous *TTN* variants in patients may yield subclinical phenotypes similar to that seen in *ttna*$^{\Delta 9/+}$ adult zebrafish (normal atrial morphology and no AF but reduced atrial contractility) that may increase the risk of AF in adulthood. Here, using homozygous

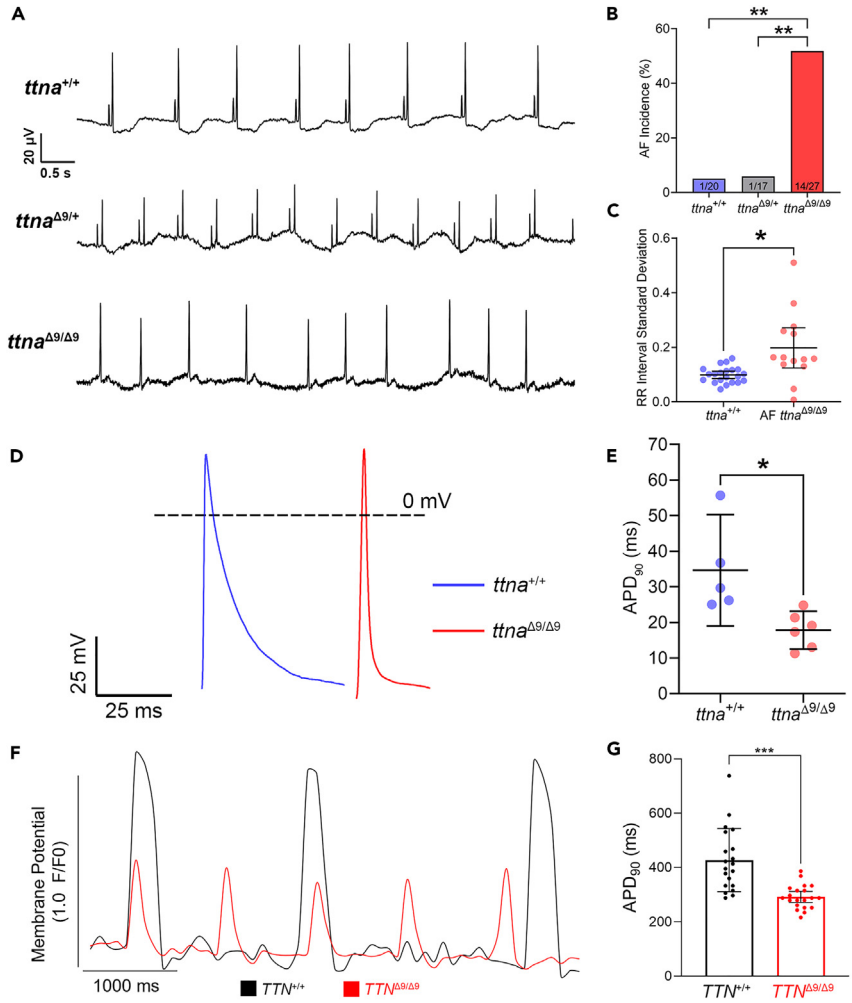

Figure 5. *ttna*$^{\Delta9/\Delta9}$ adult zebrafish exhibit atrial fibrillation (AF), and both *ttna*$^{\Delta9/\Delta9}$ zebrafish atrial cardiomyocytes and *TTN*$^{\Delta9/\Delta9}$-hiPSC-aCMs demonstrate abnormal electrophysiology

(A) Representative electrocardiogram (ECG) recordings of 7–15-months-old *ttna*$^{+/+}$ ($n = 20$), *ttna*$^{\Delta9/\Delta9}$ ($n = 17$), and *ttna*$^{\Delta9/\Delta9}$ ($n = 27$) zebrafish hearts. Upper panel: *ttna*$^{+/+}$ ECG trace; middle panel: *ttna*$^{\Delta9/+}$ ECG trace; lower panel: ttna$^{\Delta9/\Delta9}$ ECG trace demonstrating P-wave loss and arrhythmia.

(B) Quantification of AF incidence in *ttna*$^{+/+}$, *ttna*$^{\Delta9/+}$, and *ttna*$^{\Delta9/\Delta9}$ adult zebrafish.

(C) Quantification of heartbeat interval standard deviation in zebrafish with AF in comparison to *ttna*$^{+/+}$ adults.

(D) Representative recordings of action potential (AP) on isolated *ttna*$^{+/+}$ ($n = 5$) and *ttna*$^{\Delta9/\Delta9}$ ($n = 6$) zebrafish atrial cardiomyocytes at 12 months of age.

(E) Quantification of AP duration at 90% repolarization (APD_{90}) in isolated zebrafish atrial cardiomyocytes.

(F) Representative optical AP recordings of *TTN*$^{+/+}$-hiPSC-aCMs and *TTN*$^{\Delta9/\Delta9}$-hiPSC-aCMs with voltage-sensitive dye VF2.1Cl.

(G) Quantification of APD_{90} in hiPSC-aCMs ($n = 4$ independent batches, $n = 5$–6 biological replicates per batch). Data in (C, E, and G) are represented as mean ±95% confidence intervals. *$p < 0.05$; **$p < 0.01$; ***$p < 0.001$. See also Figure S8.

mutant zebrafish and hiPSC-aCMs to reveal a primary phenotype directly, we show for the first time that the *TTN*-Δ9 deletion creates an electrophysiological substrate for AF by ion channel remodeling, with I_{Ks} augmentation. The regulatory subunit KCNE1 modulates Kv7.1 channel activation by ensuring that it only opens in a specific conformation, thereby affecting voltage sensor-to-gate kinetics, and the absence of KCNE1 may facilitate new interactions between KCNQ1 and other proteins.[45,46] We found that NPPA expression in *TTN*$^{\Delta9/\Delta9}$-hiPSC-aCMs was downregulated, in contrast to the upregulation observed in *ttna*$^{\Delta9/\Delta9}$ adult zebrafish. While this downregulation was unexpected, it is striking that, in both models, the Δ9 deletion yields not only aberrant levels of NPPA/nppa and KCNQ1/KCNE1 expression but also enhanced I_{Ks} channel activity, resulting in a similar electrophysiological phenotype. Previous work has shown that there are differences in the binding of KCNE1/kcne1 to KCNQ1/kcnq1 in zebrafish as compared to mammalian I_{Ks} channels.[47] Thus, one plausible explanation for the variable NPPA/nppa expression but similar enhancement of I_{Ks} in *ttna*$^{\Delta9/\Delta9}$ adult zebrafish and *TTN*$^{\Delta9/\Delta9}$-hiPSC-aCMs may relate to different accessory proteins such as telethonin, calmodulin, PIP_2, or protein kinases binding to KCNE accessory proteins.[48] Future studies will need to determine the mechanistic differences between species, perhaps centered on divergent regulation of the I_{Ks} channel's KCNQ1 and KCNE1 subunits.

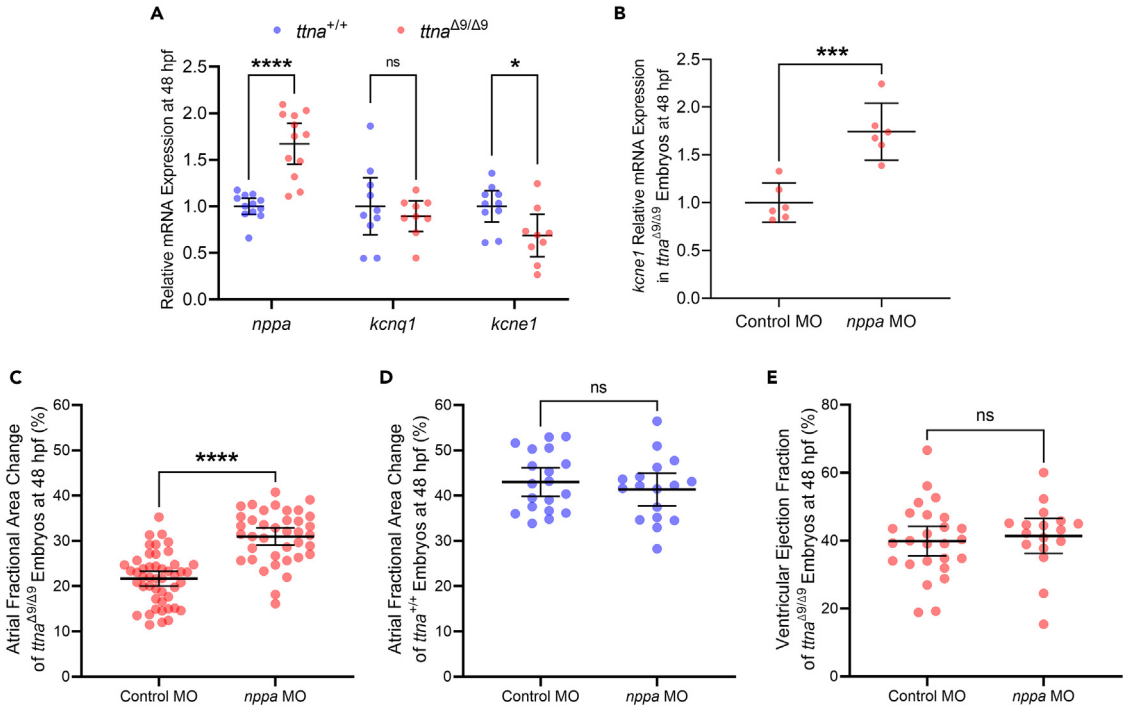

Figure 6. *ttna*$^{\Delta 9/\Delta 9}$ zebrafish embryos exhibit ANP upregulation and ANP-dependent changes in I_{Ks} channel components and atrial function

(A) Quantification of mRNA levels for *nppa*, *kcnq1*, and *kcne1* in zebrafish embryos at 48 hpf. Each dot represents a biological replicate, and each replicate contains 5–10 embryos.

(B) Quantification of mRNA levels for *kcne1* in negative control morpholino (Control MO)-treated or morpholino targeting *nppa* (*nppa* MO)-treated *ttna*$^{\Delta 9/\Delta 9}$ zebrafish embryos at 48 hpf. Each data point represents a biological replicate, and each replicate contains 5–10 embryos.

(C) Quantification for atrial contraction of Control MO-treated (n = 47) or *nppa* MO-treated (n = 38) *ttna*$^{\Delta 9/\Delta 9}$ zebrafish embryos at 48 hpf.

(D) Quantification for atrial contraction of Control MO-treated (n = 19) or *nppa* MO-treated (n = 17) *ttna*$^{+/+}$ zebrafish embryos at 48 hpf.

(E) Quantification of ventricular contraction of Control MO-treated (n = 26) or *nppa* MO-treated (n = 17) *ttna*$^{\Delta 9/\Delta 9}$ zebrafish embryos at 48 hpf. Data are represented as mean ±95% confidence intervals. ns $p > 0.05$; *$p < 0.05$; ***$p < 0.001$; ****$p < 0.0001$. See also Figures S9 and S10.

Given the known contributions of titin in ventricular cardiomyocytes and skeletal muscle, it is intriguing that the primary, persistent effect of the Δ9 deletion is atria specific. Ahlberg et al.[16] previously suggested that increased atrial fibrosis in adult zebrafish carrying an N-terminal *TTN*tv was an important risk factor for the development of AF. However, *ttna/TTN*-Δ9 failed to show significant fibrosis in both zebrafish and mature hiPSC-aCMs, suggesting domain-specific differences in pathogenesis and a novel role for the Δ9 region in driving AF independent of atrial fibrosis. While *ttna*$^{\Delta 9/\Delta 9}$ zebrafish ventricles recover rapidly, persistent atrial defects accompanied by ANP overexpression suggest that, in line with previous studies,[35,40] ANP increases I_{Ks} and leads to AF, providing an atrial-specific mechanistic link between developmental defects and adult AF that is further strengthened by the absence of a skeletal muscle phenotype. Additionally, adult *ttna*$^{\Delta 9/\Delta 9}$ zebrafish exhibit atrial-specific sarcomere disorganization, perhaps due to the long-term effects of persistent weak atrial contraction and/or compensatory structural remodeling. It will be interesting to see if future studies identify atrial-specific titin-binding partners that contribute to sarcomere instability over time. We also showed that the Δ9 deletion leads to markedly reduced cTnT expression in *TTN*$^{\Delta 9/\Delta 9}$-hiPSC-aCMs. While studies have shown that cTnT is essential in sarcomere assembly and cardiac contractility in the ventricles,[49] it is intriguing that our 9 amino acid deletion in the A-band of titin leads to sarcomeric defects and reduced contractility in the atria instead.

Mature *TTN*-Δ9-hiPSC-aCMs displayed pathologies closely resembling those exhibited by patients harboring *TTN*tvs, including AF, atrial cardiomyopathy, sarcomere disassembly, abnormal myocardial relaxation, and reduced contractility. Our analyses of matured *TTN*-Δ9-hiPSC-aCMs revealed markedly compromised cardiac tissue integrity by TEM analysis. The mechanisms whereby some *TTN*tvs cause dilated cardiomyopathy while others predispose to AF remain unclear, and pleiotropic variability in titin-linked disease may relate to chamber- or disease-specific interactions between titin and a variety of cardiac-associated partners. Our findings connecting titin to I_{Ks}, and AF may stimulate future work that integrates multiple signaling pathways to provide a holistic view of how cardiac development impacts AF in adults. Of note, PITX2 regulates ion channel gene expression during cardiac development in both zebrafish and mice,[44,50,51] and this transcription factor may play a key role alongside titin in ion channel regulation. Another potential contributor is Four and a Half LIM domains 2 (FHL2), which has been suggested to bind to titin's M-line[52] and, separately, to interact with I_{Ks} and affect its activity.[53] Thus, there may be a number of signaling mechanisms that work in concert to connect structural proteins to ion channel modulation and the regulation of atrial rhythmicity.

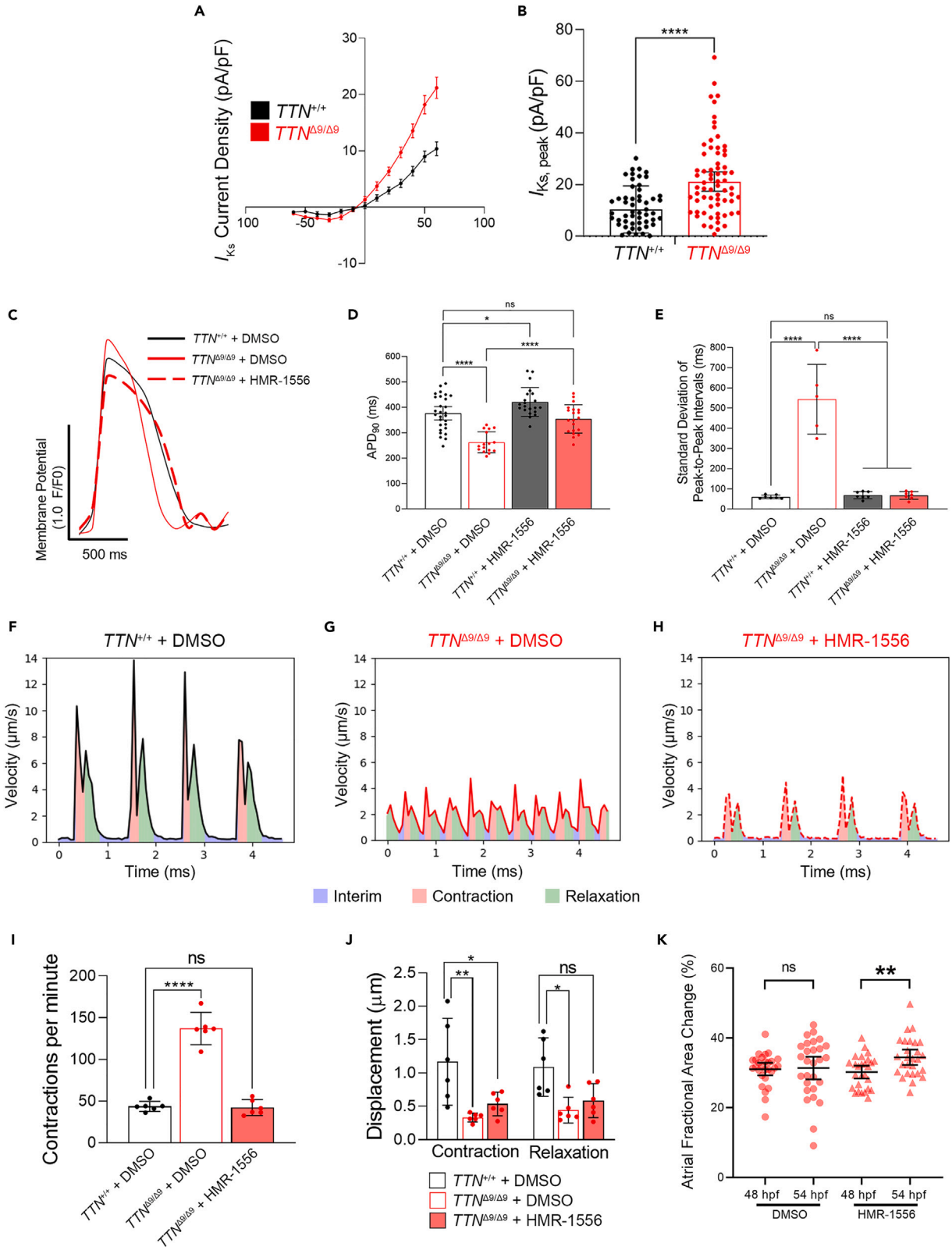
A
B
C
D
E
F
G
H
I
J
K
Current Density (pA/pF)
I_{Ks}
$TTN^{+/+}$
$TTN^{\Delta 9/\Delta 9}$
$I_{Ks,\ peak}$ (pA/pF)
****
$TTN^{+/+}$ + DMSO
$TTN^{\Delta 9/\Delta 9}$ + DMSO
$TTN^{\Delta 9/\Delta 9}$ + HMR-1556
Membrane Potential (1.0 F/F0)
500 ms
APD_{90} (ms)
ns
*
Standard Deviation of Peak-to-Peak Intervals (ms)
Velocity (µm/s)
Time (ms)
Interim
Contraction
Relaxation
Contractions per minute
Displacement (µm)
Contraction
Relaxation
Atrial Fractional Area Change (%)
**
48 hpf
54 hpf
DMSO
HMR-1556

Figure 7. Targeted pharmacological blockade of I_{Ks} rescues the arrhythmia and improves contraction and relaxation in *TTN*$^{\Delta 9/\Delta 9}$-hiPSC-aCMs and *ttna*$^{\Delta 9/\Delta 9}$ zebrafish atria

(A and B) High-throughput voltage clamping showing I_{Ks} in *TTN*$^{\Delta 9/\Delta 9}$-hiPSC-aCMs ($n = 71$) compared to *TTN*$^{+/+}$-hiPSC-aCMs ($n = 59$): current-voltage (I-V) curves (A) and quantification of I_{Ks} densities at +60 mV (B).

(C) Representative optical action potential recordings of *TTN*$^{+/+}$-hiPSC-aCMs and *TTN*$^{\Delta 9/\Delta 9}$-hiPSC-aCMs treated with either vehicle (DMSO) or HMR-1556 in DMSO.

(D and E) Quantification of APD_{90} (D) and contraction rhythm (E) of DMSO- or HMR-1556/DMSO-treated *TTN*$^{+/+}$-hiPSC-aCMs and *TTN*$^{\Delta 9/\Delta 9}$-hiPSC-aCMs. ($n = 3$ independent batches, $n = 5$–9 biological replicates per batch).

(F–H) Representative recordings of contractility analysis on hiPSC-aCMs treated with DMSO or HMR-1556/DMSO.

(I and J) Quantification of contractility parameters including contraction frequency (I, 1-way ANOVA with Bonferroni's correction) and displacement (J, two-way ANOVA with Bonferroni's correction, $n = 3$ independent batches, $n = 2$ biological replicates per batch).

(K) Quantification of *ttna*$^{\Delta 9/\Delta 9}$ zebrafish embryo atrial contraction under either DMSO ($n = 28$) or 10 μM HMR-1556/DMSO ($n = 27$) treatment from 50 to 54 hpf. Data in (A, B, D–E, and I–K) are represented as mean ±95% confidence intervals. ns $p > 0.05$; *$p < 0.05$; **$p < 0.01$; ****$p < 0.0001$. See also Figures S11–S13.

Patients harboring *TTN*tvs are at increased risk of developing dilated cardiomyopathy and cardiac arrhythmias, but there is an incomplete understanding of the underlying mechanisms and the implications for broadly effective therapies. Childhood atrial function has not been studied in patients carrying *TTN*tvs and is not routinely evaluated, leaving open the possibility that congenital defects could give rise to AF predisposition at an early age, particularly in combination with risk factors such as atrial dilatation.[54] Meanwhile, the clinical relevance of many missense variants in titin remains unclear.[55] Strikingly, our I_{Ks} blockade in zebrafish and mature hiPSC-aCMs not only prevented AF but also improved atrial function in embryos, which has potential clinical implications for both pediatric and adult patients. As titin serves as an electromechanical bridge connecting sarcomeric structures with ion channels, developing drug treatments targeting ion channel remodeling may not only restore and maintain sinus rhythm and improve contractility but also improve the long-term outcome for patients who harbor disease-causing rare variants in titin or other sarcomeric proteins by reducing the risk of thromboembolic complications.

Limitations of the study

While the zebrafish serves as a robust model system for cardiovascular research, differences such as the number of heart chambers limit the degree to which human disease-relevant conclusions can be drawn. Similarly, at the molecular level, ANP expression appears to be regulated differently between zebrafish and hiPSC-aCMs, complicating investigation of divergent mechanisms but also offering opportunities for future comparative studies. Finally, the structure of the domain containing the Δ9 deletion has not been solved due to titin's large size, limiting the ability to predict and determine Δ9's effect on titin's binding partners.

STAR★METHODS

Detailed methods are provided in the online version of this paper and include the following:

- KEY RESOURCES TABLE
- RESOURCE AVAILABILITY
  - Lead contact
  - Materials availability
  - Data and code availability
- EXPERIMENTAL MODEL AND STUDY PARTICIPANT DETAILS
  - Zebrafish model
  - Human induced pluripotent stem cell-derived atrial cardiomyocytes (hiPSC-aCM) model
- METHOD DETAILS
  - *In situ* hybridization chain reaction (HCR)
  - Zebrafish transmission electron microscopy
  - Zebrafish adult survival determination
  - Zebrafish live imaging and cardiac parameter measurements
  - Zebrafish adult heart dissection and histology
  - Adult heart size measurement
  - Zebrafish adult echocardiography
  - Zebrafish adult electrocardiography (ECG)
  - Zebrafish proteomics analysis
  - Electrophysiological recording of zebrafish atrial cardiomyocytes
  - Zebrafish morpholino treatment
  - Zebrafish embryo drug treatment
  - Immunofluorescence cellular preparation, imaging, and analysis
  - Transmission electron microscopy (TEM) sample preparation
  - Contractility analysis

- Myocyte isolation for automated electrophysiology
- Automated electrophysiology
- Data analysis for automated electrophysiology
- Optical voltage mapping and drug exposures

- QUANTIFICATION AND STATISTICAL ANALYSIS

SUPPLEMENTAL INFORMATION

Supplemental information can be found online at https://doi.org/10.1016/j.isci.2024.110395.

ACKNOWLEDGMENTS

We thank Dr. Ana Beiriger for creating the model figure. Research funding was provided by National Institutes of Health R01HL138737, R01HL150586, R01HL148444, 5R35GM133416, and 5T32HL139439 and by UAB Heersink School of Medicine Start-Up Funds. This work made use of the instruments and services provided by the Electron Microscopy Core, Research Histology Core, Genomics Research Core, and Cardiovascular Research Core all in the University of Illinois Chicago's Research Resources Center, established with the support of the Vice Chancellor of Research.

AUTHOR CONTRIBUTIONS

Conceptualization, X.J., O.T.L., D.D., and A.Saxena; methodology, X.J., O.T.L., D.T., Y.G., D.D., and A.Saxena; formal analysis, X.J., O.T.L., Z.Z., B.A.I., M.A.P., A.Sridhar, D.T., A.Swick, C.G.V., and J.R.; investigation, X.J., O.T.L., H.C., Z.Z., B.A.I., M.A.P., G.E.B., A.Sridhar, D.T., A.Swick, R.M., C.G.V., and F.N.; resources, S.R.K., Y.G., D.D., and A.Saxena; writing – original draft, X.J., O.T.L., D.D., and A.Saxena; writing – review and editing, X.J., O.T.L., D.T., C.G.V., A.L.G., S.R.K., J.R., D.D., and A.Saxena; visualization, X.J., O.T.L., Z.Z., and A.Saxena; supervision, A.L.G., S.R.K., Y.G., D.D., and A.Saxena; funding acquisition, S.R.K., Y.G., D.D., and A.Saxena

DECLARATION OF INTERESTS

The authors declare no competing interests.

Received: March 14, 2024
Revised: May 28, 2024
Accepted: June 25, 2024
Published: June 27, 2024

REFERENCES

1. Virani, S.S., Alonso, A., Aparicio, H.J., Benjamin, E.J., Bittencourt, M.S., Callaway, C.W., Carson, A.P., Chamberlain, A.M., Cheng, S., Delling, F.N., et al. (2021). Heart disease and stroke statistics—2021 update: a report from the American Heart Association. Circulation *143*, e254–e743.
2. Xintarakou, A., Tzeis, S., Psarras, S., Asvestas, D., and Vardas, P. (2020). Atrial fibrosis as a dominant factor for the development of atrial fibrillation: facts and gaps. Europace *22*, 342–351. https://doi.org/10.1093/europace/euaa009.
3. Kornej, J., Börschel, C.S., Benjamin, E.J., and Schnabel, R.B. (2020). Epidemiology of Atrial Fibrillation in the 21st Century: Novel Methods and New Insights. Circ. Res. *127*, 4–20. https://doi.org/10.1161/CIRCRESAHA.120.316340.
4. Roselli, C., Chaffin, M.D., Weng, L.C., Aeschbacher, S., Ahlberg, G., Albert, C.M., Almgren, P., Alonso, A., Anderson, C.D., Aragam, K.G., et al. (2018). Multi-ethnic genome-wide association study for atrial fibrillation. Nat. Genet. *50*, 1225–1233. https://doi.org/10.1038/s41588-018-0133-9.
5. Nielsen, J.B., Thorolfsdottir, R.B., Fritsche, L.G., Zhou, W., Skov, M.W., Graham, S.E., Herron, T.J., McCarthy, S., Schmidt, E.M., Sveinbjornsson, G., et al. (2018). Biobank-driven genomic discovery yields new insight into atrial fibrillation biology. Nat. Genet. *50*, 1234–1239. https://doi.org/10.1038/s41588-018-0171-3.
6. Fatkin, D., Santiago, C.F., Huttner, I.G., Lubitz, S.A., and Ellinor, P.T. (2017). Genetics of Atrial Fibrillation: State of the Art in 2017. Heart Lung Circ. *26*, 894–901. https://doi.org/10.1016/j.hlc.2017.04.008.
7. Holm, H., Gudbjartsson, D.F., Sulem, P., Masson, G., Helgadottir, H.T., Zanon, C., Magnusson, O.T., Helgason, A., Saemundsdottir, J., Gylfason, A., et al. (2011). A rare variant in MYH6 is associated with high risk of sick sinus syndrome. Nat. Genet. *43*, 316–320. https://doi.org/10.1038/ng.781.
8. Gudbjartsson, D.F., Holm, H., Sulem, P., Masson, G., Oddsson, A., Magnusson, O.T., Saemundsdottir, J., Helgadottir, H.T., Helgason, H., Johannsdottir, H., et al. (2017). A frameshift deletion in the sarcomere gene MYL4 causes early-onset familial atrial fibrillation. Eur. Heart J. *38*, 27–34. https://doi.org/10.1093/eurheartj/ehw379.
9. Ghazizadeh, Z., Kiviniemi, T., Olafsson, S., Plotnick, D., Beerens, M.E., Zhang, K., Gillon, L., Steinbaugh, M.J., Barrera, V., Sui, S.H., et al. (2020). Metastable Atrial State Underlies the Primary Genetic Substrate for MYL4 Mutation-Associated Atrial Fibrillation. Circulation *141*, 301–312. https://doi.org/10.1161/CIRCULATIONAHA.119.044268.
10. Yoneda, Z.T., Anderson, K.C., Quintana, J.A., O'Neill, M.J., Sims, R.A., Glazer, A.M., Shaffer, C.M., Crawford, D.M., Stricker, T., Ye, F., et al. (2021). Early-Onset Atrial Fibrillation and the Prevalence of Rare Variants in Cardiomyopathy and Arrhythmia Genes. JAMA Cardiol. *6*, 1371–1379. https://doi.org/10.1001/jamacardio.2021.3370.
11. Yoneda, Z.T., Anderson, K.C., Ye, F., Quintana, J.A., O'Neill, M.J., Sims, R.A., Sun, L., Glazer, A.M., Davogustto, G., El-Harasis, M., et al. (2022). Mortality Among Patients With Early-Onset Atrial Fibrillation and Rare Variants in Cardiomyopathy and Arrhythmia Genes. JAMA Cardiol. *7*, 733–741. https://doi.org/10.1001/jamacardio.2022.0810.
12. Linke, W.A., and Hamdani, N. (2014). Gigantic business: titin properties and function through thick and thin. Circ. Res. *114*, 1052–1068. https://doi.org/10.1161/circresaha.114.301286.
13. Choi, S.H., Weng, L.C., Roselli, C., Lin, H., Haggerty, C.M., Shoemaker, M.B., Barnard, J., Arking, D.E., Chasman, D.I., Albert, C.M., et al. (2018). Association Between Titin Loss-of-Function Variants and Early-Onset Atrial Fibrillation. JAMA *320*, 2354–2364. https://doi.org/10.1001/jama.2018.18179.
14. Chalazan, B., Mol, D., Darbar, F.A., Ornelas-Loredo, A., Al-Azzam, B., Chen, Y., Tofovic, D., Sridhar, A., Alzahrani, Z., Ellinor, P., and

Darbar, D. (2021). Association of Rare Genetic Variants and Early-Onset Atrial Fibrillation in Ethnic Minority Individuals. JAMA Cardiol. *6*, 811–819. https://doi.org/10.1001/jamacardio.2021.0994.

15. Goodyer, W.R., Dunn, K., Caleshu, C., Jackson, M., Wylie, J., Moscarello, T., Platt, J., Reuter, C., Smith, A., Trela, A., et al. (2019). Broad Genetic Testing in a Clinical Setting Uncovers a High Prevalence of Titin Loss-of-Function Variants in Very Early Onset Atrial Fibrillation. Circ. Genom. Precis. Med. *12*, e002713. https://doi.org/10.1161/CIRCGEN.119.002713.
16. Ahlberg, G., Refsgaard, L., Lundegaard, P.R., Andreasen, L., Ranthe, M.F., Linscheid, N., Nielsen, J.B., Melbye, M., Haunsø, S., Sajadieh, A., et al. (2018). Rare truncating variants in the sarcomeric protein titin associate with familial and early-onset atrial fibrillation. Nat. Commun. *9*, 4316. https://doi.org/10.1038/s41467-018-06618-y.
17. Gerull, B., Gramlich, M., Atherton, J., McNabb, M., Trombitás, K., Sasse-Klaassen, S., Seidman, J.G., Seidman, C., Granzier, H., Labeit, S., et al. (2002). Mutations of TTN, encoding the giant muscle filament titin, cause familial dilated cardiomyopathy. Nat. Genet. *30*, 201–204. https://doi.org/10.1038/ng815.
18. Akinrinade, O., Koskenvuo, J.W., and Alastalo, T.-P. (2015). Prevalence of Titin Truncating Variants in General Population. PLoS One *10*, e0145284. https://doi.org/10.1371/journal.pone.0145284.
19. Franaszczyk, M., Chmielewski, P., Truszkowska, G., Stawinski, P., Michalak, E., Rydzanicz, M., Sobieszczanska-Malek, M., Pollak, A., Szczygieł, J., Kosinska, J., et al. (2017). Titin Truncating Variants in Dilated Cardiomyopathy - Prevalence and Genotype-Phenotype Correlations. PLoS One *12*, e0169007. https://doi.org/10.1371/journal.pone.0169007.
20. Corden, B., Jarman, J., Whiffin, N., Tayal, U., Buchan, R., Sehmi, J., Harper, A., Midwinter, W., Lascelles, K., Markides, V., et al. (2019). Association of Titin-Truncating Genetic Variants With Life-threatening Cardiac Arrhythmias in Patients With Dilated Cardiomyopathy and Implanted Defibrillators. JAMA Netw. Open *2*, e196520. https://doi.org/10.1001/jamanetworkopen.2019.6520.
21. Domínguez, F., Lalaguna, L., Martínez-Martín, I., Piqueras-Flores, J., Rasmussen, T.B., Zorio, E., Giovinazzo, G., Prados, B., Ochoa, J.P., Bornstein, B., et al. (2023). Titin Missense Variants as a Cause of Familial Dilated Cardiomyopathy. Circulation *147*, 1711–1713. https://doi.org/10.1161/CIRCULATIONAHA.122.062833.
22. Myhre, J.L., Hills, J.A., Prill, K., Wohlgemuth, S.L., and Pilgrim, D.B. (2014). The titin A-band rod domain is dispensable for initial thick filament assembly in zebrafish. Dev. Biol. *387*, 93–108. https://doi.org/10.1016/j.ydbio.2013.12.020.
23. Granzier, H.L., Hutchinson, K.R., Tonino, P., Methawasin, M., Li, F.W., Slater, R.E., Bull, M.M., Saripalli, C., Pappas, C.T., Gregorio, C.C., and Smith, J.E., 3rd (2014). Deleting titin's I-band/A-band junction reveals critical roles for titin in biomechanical sensing and cardiac function. Proc. Natl. Acad. Sci. USA *111*, 14589–14594. https://doi.org/10.1073/pnas.1411493111.
24. Tonino, P., Kiss, B., Strom, J., Methawasin, M., Smith, J.E., Kolb, J., Labeit, S., and Granzier, H. (2017). The giant protein titin regulates the length of the striated muscle thick filament. Nat. Commun. *8*, 1041. https://doi.org/10.1038/s41467-017-01144-9.
25. Hoffman, J.I.E., and Kaplan, S. (2002). The incidence of congenital heart disease. J. Am. Coll. Cardiol. *39*, 1890–1900. https://doi.org/10.1016/S0735-1097(02)01886-7.
26. de Miguel, I.M., and Ávila, P. (2021). Atrial Fibrillation in Congenital Heart Disease. Eur. Cardiol. *16*, e06. https://doi.org/10.15420/ecr.2020.41.
27. Ebrahim, M.A., Escudero, C.A., Kantoch, M.J., Vondermuhll, I.F., and Atallah, J. (2018). Insights on Atrial Fibrillation in Congenital Heart Disease. Can. J. Cardiol. *34*, 1531–1533. https://doi.org/10.1016/j.cjca.2018.08.010.
28. Waldmann, V., Laredo, M., Abadir, S., Mondésert, B., and Khairy, P. (2019). Atrial fibrillation in adults with congenital heart disease. Int. J. Cardiol. *287*, 148–154. https://doi.org/10.1016/j.ijcard.2019.01.079.
29. Hong, L., Zhang, M., Ly, O.T., Chen, H., Sridhar, A., Lambers, E., Chalazan, B., Youn, S.W., Maienschein-Cline, M., Feferman, L., et al. (2021). Human induced pluripotent stem cell-derived atrial cardiomyocytes carrying an SCN5A mutation identify nitric oxide signaling as a mediator of atrial fibrillation. Stem Cell Rep. *16*, 1542–1554. https://doi.org/10.1016/j.stemcr.2021.04.019.
30. Ly, O.T., Chen, H., Brown, G.E., Hong, L., Wang, X., Han, Y.D., Pavel, M.A., Sridhar, A., Maienschein-Cline, M., Chalazan, B., et al. (2022). Mutant ANP induces mitochondrial and ion channel remodeling in a human iPSC-derived atrial fibrillation model. JCI Insight *7*, e155640. https://doi.org/10.1172/jci.insight.155640.
31. Seeley, M., Huang, W., Chen, Z., Wolff, W.O., Lin, X., and Xu, X. (2007). Depletion of zebrafish titin reduces cardiac contractility by disrupting the assembly of Z-discs and A-bands. Circ. Res. *100*, 238–245.
32. Bang, M.L., Centner, T., Fornoff, F., Geach, A.J., Gotthardt, M., McNabb, M., Witt, C.C., Labeit, D., Gregorio, C.C., Granzier, H., and Labeit, S. (2001). The complete gene sequence of titin, expression of an unusual approximately 700-kDa titin isoform, and its interaction with obscurin identify a novel Z-line to I-band linking system. Circ. Res. *89*, 1065–1072. https://doi.org/10.1161/hh2301.100981.
33. Mikelsaar, A.V., Sunter, A., Mikelsaar, R., Toomik, P., Koiveer, A., Mikelsaar, I., and Juronen, E. (2012). Epitope of titin A-band-specific monoclonal antibody Tit1 5 H1.1 is highly conserved in several Fn3 domains of the titin molecule. Centriole staining in human, mouse and zebrafish cells. Cell Div. *7*, 21. https://doi.org/10.1186/1747-1028-7-21.
34. Yang, J., Shih, Y.H., and Xu, X. (2014). Understanding cardiac sarcomere assembly with zebrafish genetics. Anat. Rec. *297*, 1681–1693. https://doi.org/10.1002/ar.22975.
35. Ly, O.T., Chen, H., Brown, G.E., Hong, L., Wang, X., Han, Y.D., Pavel, M.A., Sridhar, A., Maienschein-Cline, M., Chalazan, B., et al. (2022). Mutant ANP induces mitochondrial and ion channel remodeling in a human iPSC–derived atrial fibrillation model. JCI insight *7*, e155640.
36. Brown, G.E., Han, Y.D., Michell, A.R., Ly, O.T., Vanoye, C.G., Spanghero, E., George, A.L., Darbar, D., and Khetani, S.R. (2024). Engineered cocultures of iPSC-derived atrial cardiomyocytes and atrial fibroblasts for modeling atrial fibrillation. Sci. Adv. *10*, eadg1222. https://doi.org/10.1126/sciadv.adg1222.
37. Man, J., Barnett, P., and Christoffels, V.M. (2018). Structure and function of the Nppa-Nppb cluster locus during heart development and disease. Cell. Mol. Life Sci. *75*, 1435–1444. https://doi.org/10.1007/s00018-017-2737-0.
38. Sergeeva, I.A., Hooijkaas, I.B., Van Der Made, I., Jong, W.M.C., Creemers, E.E., and Christoffels, V.M. (2014). A transgenic mouse model for the simultaneous monitoring of ANF and BNP gene activity during heart development and disease. Cardiovasc. Res. *101*, 78–86. https://doi.org/10.1093/cvr/cvt228.
39. Guo, J., Gan, X.T., Haist, J.V., Rajapurohitam, V., Zeidan, A., Faruq, N.S., and Karmazyn, M. (2011). Ginseng Inhibits Cardiomyocyte Hypertrophy and Heart Failure via NHE-1 Inhibition and Attenuation of Calcineurin Activation. Circ. Heart Fail. *4*, 79–88. https://doi.org/10.1161/CIRCHEARTFAILURE.110.957969.
40. Menon, A., Hong, L., Savio-Galimberti, E., Sridhar, A., Youn, S.W., Zhang, M., Kor, K., Blair, M., Kupershmidt, S., and Darbar, D. (2019). Electrophysiologic and molecular mechanisms of a frameshift NPPA mutation linked with familial atrial fibrillation. J. Mol. Cell. Cardiol. *132*, 24–35. https://doi.org/10.1016/j.yjmcc.2019.05.004.
41. Barhanin, J., Lesage, F., Guillemare, E., Fink, M., Lazdunski, M., and Romey, G. (1996). K(V)LQT1 and lsK (minK) proteins associate to form the I(Ks) cardiac potassium current. Nature *384*, 78–80.
42. Sanguinetti, M.C., Curran, M.E., Zou, A., Shen, J., Spector, P.S., Atkinson, D.L., and Keating, M.T. (1996). Coassembly of K(V)LQT1 and minK (IsK) proteins to form cardiac I(Ks) potassium channel. Nature *384*, 80–83. https://doi.org/10.1038/384080a0.
43. Wu, X., and Larsson, H.P. (2020). Insights into Cardiac IKs (KCNQ1/KCNE1) Channels Regulation. Int. J. Mol. Sci. *21*, 9440. https://doi.org/10.3390/ijms21249440.
44. Collins, M.M., Ahlberg, G., Hansen, C.V., Guenther, S., Marín-Juez, R., Sokol, A.M., El-Sammak, H., Piesker, J., Hellsten, Y., Olesen, M.S., et al. (2019). Early sarcomere and metabolic defects in a zebrafish pitx2c cardiac arrhythmia model. Proc. Natl. Acad. Sci. USA *116*, 24115–24121.
45. Barro-Soria, R., Ramentol, R., Liin, S.I., Perez, M.E., Kass, R.S., and Larsson, H.P. (2017). KCNE1 and KCNE3 modulate KCNQ1 channels by affecting different gating transitions. Proc. Natl. Acad. Sci. USA *114*, E7367–E7376. https://doi.org/10.1073/pnas.1710335114.
46. Temple, J., Frias, P., Rottman, J., Yang, T., Wu, Y., Verheijck, E.E., Zhang, W., Siprachanh, C., Kanki, H., Atkinson, J.B., et al. (2005). Atrial Fibrillation in KCNE1-Null Mice. Circ. Res. *97*, 62–69. https://doi.org/10.1161/01.RES.0000173047.42236.88.
47. Haverinen, J., Hassinen, M., and Vornanen, M. (2022). Effect of channel assembly (KCNQ1 or KCNQ1+ KCNE1) on the response of zebrafish IKs current to IKs inhibitors and activators. J. Cardiovasc. Pharmacol. *79*, 670–677.
48. Sanguinetti, M.C., and Seebohm, G. (2021). Physiological Functions, Biophysical Properties, and Regulation of KCNQ1 (KV7.1) Potassium Channels. In Ion Channels in Biophysics and Physiology, L. Zhou, ed. (Springer Nature Singapore), pp. 335–353. https://doi.org/10.1007/978-981-16-4254-8_15.
49. Sehnert, A.J., Huq, A., Weinstein, B.M., Walker, C., Fishman, M., and Stainier, D.Y. (2002). Cardiac troponin T is essential in

sarcomere assembly and cardiac contractility. Nat. Genet. *31*, 106–110.
50. Tao, Y., Zhang, M., Li, L., Bai, Y., Zhou, Y., Moon, A.M., Kaminski, H.J., and Martin, J.F. (2014). Pitx2, an atrial fibrillation predisposition gene, directly regulates ion transport and intercalated disc genes. Circ. Cardiovasc. Genet. *7*, 23–32.
51. Nadadur, R.D., Broman, M.T., Boukens, B., Mazurek, S.R., Yang, X., Van Den Boogaard, M., Bekeny, J., Gadek, M., Ward, T., Zhang, M., et al. (2016). Pitx2 modulates a Tbx5-dependent gene regulatory network to maintain atrial rhythm. Sci. Transl. Med. *8*, 354ra115.
52. Lange, S., Auerbach, D., McLoughlin, P., Perriard, E., Schäfer, B.W., Perriard, J.-C., and Ehler, E. (2002). Subcellular targeting of metabolic enzymes to titin in heart muscle may be mediated by DRAL/FHL-2. J. Cell Sci. *115*, 4925–4936.
53. Kupershmidt, S., Yang, I.C.-H., Sutherland, M., Wells, K.S., Yang, T., Yang, P., Balser, J.R., and Roden, D.M. (2002). Cardiac-enriched LIM domain protein fhl2 is required to generate I Ks in a heterologous system. Cardiovasc. Res. *56*, 93–103.
54. Darbar, D., and Roden, D.M. (2013). Genetic mechanisms of atrial fibrillation: impact on response to treatment. Nat. Rev. Cardiol. *10*, 317–329.
55. Akinrinade, O., Heliö, T., Lekanne Deprez, R.H., Jongbloed, J.D., Boven, L.G., van den Berg, M.P., Pinto, Y.M., Alastalo, T.-P., Myllykangas, S., and Spaendonck-Zwarts, K.v. (2019). Relevance of titin missense and non-frameshifting insertions/deletions variants in dilated cardiomyopathy. Sci. Rep. *9*, 1–9.
56. Huang, C.-J., Tu, C.-T., Hsiao, C.-D., Hsieh, F.-J., and Tsai, H.-J. (2003). Germ-line transmission of a myocardium-specific GFP transgene reveals critical regulatory elements in the cardiac myosin light chain 2 promoter of zebrafish. Dev. Dyn. *228*, 30–40. https://doi.org/10.1002/dvdy.10356.
57. Traver, D., Paw, B.H., Poss, K.D., Penberthy, W.T., Lin, S., and Zon, L.I. (2003). Transplantation and in vivo imaging of multilineage engraftment in zebrafish bloodless mutants. Nat. Immunol. *4*, 1238–1246. https://doi.org/10.1038/ni1007.
58. Becker, J.R., Chatterjee, S., Robinson, T.Y., Bennett, J.S., Panáková, D., Galindo, C.L., Zhong, L., Shin, J.T., Coy, S.M., Kelly, A.E., et al. (2014). Differential activation of natriuretic peptide receptors modulates cardiomyocyte proliferation during development. Development *141*, 335–345. https://doi.org/10.1242/dev.100370.
59. Labun, K., Montague, T.G., Krause, M., Torres Cleuren, Y.N., Tjeldnes, H., and Valen, E. (2019). CHOPCHOP v3: expanding the CRISPR web toolbox beyond genome editing. Nucleic Acids Res. *47*, W171–W174.
60. Schindelin, J., Arganda-Carreras, I., Frise, E., Kaynig, V., Longair, M., Pietzsch, T., Preibisch, S., Rueden, C., Saalfeld, S., Schmid, B., et al. (2012). Fiji: an open-source platform for biological-image analysis. Nat. Methods *9*, 676–682. https://doi.org/10.1038/nmeth.2019.
61. Kimmel, C.B., Ballard, W.W., Kimmel, S.R., Ullmann, B., and Schilling, T.F. (1995). Stages of embryonic development of the zebrafish. Dev. Dyn. *203*, 253–310. https://doi.org/10.1002/aja.1002030302.
62. Westerfield, M. (2000). The Zebrafish Book. A Guide for the Laboratory Use of Zebrafish (Danio rerio), 4th Edition (Univ. of Oregon Press)).
63. Essner, J. (2016). Zebrafish embryo microinjection Ribonucleoprotein delivery using the Alt-R™ CRISPR-Cas9 System. https://sfvideo.blob.core.windows.net/sitefinity/docs/default-source/user-submitted-method/crispr-cas9-rnp-delivery-zebrafish-embryos-j-essnerc46b5a1532796e2eaa53ff00001c1b3c.pdf?sfvrsn=52123407_10.
64. Argenziano, M., Lambers, E., Hong, L., Sridhar, A., Zhang, M., Chalazan, B., Menon, A., Savio-Galimberti, E., Wu, J.C., Rehman, J., and Darbar, D. (2018). Electrophysiologic Characterization of Calcium Handling in Human Induced Pluripotent Stem Cell-Derived Atrial Cardiomyocytes. Stem Cell Rep. *10*, 1867–1878. https://doi.org/10.1016/j.stemcr.2018.04.005.
65. Devalla, H.D., Schwach, V., Ford, J.W., Milnes, J.T., El-Haou, S., Jackson, C., Gkatzis, K., Elliott, D.A., Chuva de Sousa Lopes, S.M., Mummery, C.L., et al. (2015). Atrial-like cardiomyocytes from human pluripotent stem cells are a robust preclinical model for assessing atrial-selective pharmacology. EMBO Mol. Med. *7*, 394–410. https://doi.org/10.15252/emmm.201404757.
66. Choi, H.M.T., Schwarzkopf, M., Fornace, M.E., Acharya, A., Artavanis, G., Stegmaier, J., Cunha, A., and Pierce, N.A. (2018). Third-generation in situ hybridization chain reaction: multiplexed, quantitative, sensitive, versatile, robust. Development *145*, dev165753. https://doi.org/10.1242/dev.165753.
67. Treffy, R.W., Rajan, S.G., Jiang, X., Nacke, L.M., Malkana, U.A., Naiche, L., Bergey, D.E., Santana, D., Rajagopalan, V., Kitajewski, J.K., et al. (2021). Neuroblastoma differentiation in vivo excludes cranial tumors. Dev. Cell *56*, 2752–2764.e6.
68. Singleman, C., and Holtzman, N.G. (2011). Heart dissection in larval, juvenile and adult zebrafish, Danio rerio. J. Vis. Exp. *3165*, 3165. https://doi.org/10.3791/3165.
69. Gaur, H., Pullaguri, N., Nema, S., Purushothaman, S., Bhargava, Y., and Bhargava, A. (2018). ZebraPace: an open-source method for cardiac-rhythm estimation in untethered zebrafish larvae. Zebrafish *15*, 254–262.
70. Yalcin, H.C., Amindari, A., Butcher, J.T., Althani, A., and Yacoub, M. (2017). Heart function and hemodynamic analysis for zebrafish embryos. Dev. Dyn. *246*, 868–880. https://doi.org/10.1002/dvdy.24497.
71. Vermot, J., Forouhar, A.S., Liebling, M., Wu, D., Plummer, D., Gharib, M., and Fraser, S.E. (2009). Reversing Blood Flows Act through klf2a to Ensure Normal Valvulogenesis in the Developing Heart. PLoS Biol. *7*, e1000246. https://doi.org/10.1371/journal.pbio.1000246.
72. Evangelisti, A., Schimmel, K., Joshi, S., Shah, K., Fisch, S., Alexander, K.M., Liao, R., and Morgado, I. (2020). High-Frequency Ultrasound Echocardiography to Assess Zebrafish Cardiac Function. J. Vis. Exp. *157*, e60976. https://doi.org/10.3791/60976.
73. Niimi, A.J. (1975). Relationship of body surface area to weight in fishes. Can. J. Zool. *53*, 1192–1194. https://doi.org/10.1139/z75-141.
74. Yan, J., Li, H., Bu, H., Jiao, K., Zhang, A.X., Le, T., Cao, H., Li, Y., Ding, Y., and Xu, X. (2020). Aging-associated sinus arrest and sick sinus syndrome in adult zebrafish. PLoS One *15*, e0232457.
75. Linscheid, N., Santos, A., Poulsen, P.C., Mills, R.W., Calloe, K., Leurs, U., Ye, J.Z., Stolte, C., Thomsen, M.B., Bentzen, B.H., et al. (2021). Quantitative proteome comparison of human hearts with those of model organisms. PLoS Biol. *19*, e3001144.
76. Kong, A.T., Leprevost, F.V., Avtonomov, D.M., Mellacheruvu, D., and Nesvizhskii, A.I. (2017). MSFragger: ultrafast and comprehensive peptide identification in mass spectrometry–based proteomics. Nat. Methods *14*, 513–520.
77. Perez-Riverol, Y., Bai, J., Bandla, C., García-Seisdedos, D., Hewapathirana, S., Kamatchinathan, S., Kundu, D.J., Prakash, A., Frericks-Zipper, A., Eisenacher, M., et al. (2022). The PRIDE database resources in 2022: a hub for mass spectrometry-based proteomics evidences. Nucleic Acids Res. *50*, D543–D552. https://doi.org/10.1093/nar/gkab1038.
78. Sander, V., Sune, G., Jopling, C., Morera, C., and Izpisua Belmonte, J.C. (2013). Isolation and in vitro culture of primary cardiomyocytes from adult zebrafish hearts. Nat. Protoc. *8*, 800–809. https://doi.org/10.1038/nprot.2013.041.
79. Kamel, S.M., van Opbergen, C.J.M., Koopman, C.D., Verkerk, A.O., Boukens, B.J.D., de Jonge, B., Onderwater, Y.L., van Alebeek, E., Chocron, S., Polidoro Pontalti, C., et al. (2021). Istaroxime treatment ameliorates calcium dysregulation in a zebrafish model of phospholamban R14del cardiomyopathy. Nat. Commun. *12*, 7151. https://doi.org/10.1038/s41467-021-27461-8.
80. Brette, F., Luxan, G., Cros, C., Dixey, H., Wilson, C., and Shiels, H.A. (2008). Characterization of isolated ventricular myocytes from adult zebrafish (Danio rerio). Biochem. Biophys. Res. Commun. *374*, 143–146. https://doi.org/10.1016/j.bbrc.2008.06.109.
81. Arganda-Carreras, I., Fernandez-Gonzalez, R., Munoz-Barrutia, A., and Ortiz-De-Solorzano, C. (2010). 3D reconstruction of histological sections: Application to mammary gland tissue. Microsc. Res. Tech. *73*, 1019–1029. https://doi.org/10.1002/jemt.20829.
82. Farneback, G., and Westin, C.F. (2006). Affine and deformable registration based on polynomial expansion. Med. Image Comput. Comput. Assist Interv. *9*, 857–864. https://doi.org/10.1007/11866565_105.
83. Breiman, L. (1999). Prediction games and arcing algorithms. Neural Comput. *11*, 1493–1517. https://doi.org/10.1162/089976699300016106.
84. Pedregosa, F., Eickenberg, M., Ciuciu, P., Thirion, B., and Gramfort, A. (2015). Data-driven HRF estimation for encoding and decoding models. Neuroimage *104*, 209–220. https://doi.org/10.1016/j.neuroimage.2014.09.060.
85. Goldfracht, I., Efraim, Y., Shinnawi, R., Kovalev, E., Huber, I., Gepstein, A., Arbel, G., Shaheen, N., Tiburcy, M., Zimmermann, W.H., et al. (2019). Engineered heart tissue models from hiPSC-derived cardiomyocytes and cardiac ECM for disease modeling and drug testing applications. Acta Biomater. *92*, 145–159.

STAR★METHODS

KEY RESOURCES TABLE

REAGENT or RESOURCE	SOURCE	IDENTIFIER
Antibodies		
Anti-Natriuretic peptides A antibody [EPR20247]	Abcam	Cat#ab209232
anti-cTnT polyclonal (rabbit)	Abcam	Cat#ab45932; RRID:AB_956386
anti-KCNQ1 polyclonal (rabbit)	Abcam	Cat#ab181798
Chemicals, peptides, and recombinant proteins		
Tricaine/MS-222	Sigma-Aldrich	Cat#A5040
Methyl cellulose	Sigma-Aldrich	Cat#M0512
Cas9 protein	IDT	Cat#1081058
HMR-1556	Sigma-Aldrich	Cat#SML2354
Critical commercial assays		
Hybridization Chain Reaction Probes and Hairpins Version 3	Molecular Instruments	N/A
DreamTaq Hot Start Green PCR Master Mix	Thermo Scientific	Cat#K9022
LA Taq DNA polymerase	TaKaRa	Cat#RR042B
RNeasy Mini Kit	QIAGEN	Cat#74104
SuperScript IV VILO Master Mix	Invitrogen	Cat#11756050
KiCqStart SYBR Green qPCR ReadyMix	Sigma-Aldrich	Cat#KCQS00
iTaq Universal SYBR Green Supermix	Bio-Rad	Cat#1725121
Deposited data		
Adult zebrafish heart proteomics data	ProteomeXchange Consortium	PRIDE Identifier: PXD038300
Experimental models: Organisms/strains		
Zebrafish: AB wild-type	ZIRC	Cat#ZL1
Zebrafish: *Tg(cmlc2:eGFP)*	Tsai et al., 2003[56]	ZDB-TGCONSTRCT-070117-164
Zebrafish: *Tg(gata1:dsRed)*	Zon et al., 2003[57]	ZDB-TGCONSTRCT-070117-38
Oligonucleotides		
crRNA for *ttna* gRNA: AAGCTCAGTACGTTCTTCAC	IDT	N/A
TracrRNA for *ttna* gRNA	IDT	N/A
Forward primer for $ttna^{\Delta 9}$ genotyping: GCCTTCCTTCCACATTTATTTTCCA	IDT	N/A
Reverse primer for $ttna^{\Delta 9}$ genotyping: CAGGCTATCAGTGCCCATCA	IDT	N/A
Translation-blocking morpholino against *nppa*: TCAGAATTAGTCCCCCGGCCATCTC	Becker et al.[58]	N/A
Translation-blocking morpholino against *nppb*: TGTGAAGCGATTTCATGTCTCCTGA	Becker et al.[58]	N/A
Control morpholino: CCTCTTACCTCAGTTACAATTTATA	Gene Tools	SKU:PCO-StandardControl-100
gRNA for generating Δ9 deletion in *TTN*: TGTTTCAGATGTTGCAATCA	IDT	N/A
HDR template for generating Δ9 deletion in *TTN*: CAATCATTGCACGCTTACTAATATCCTGGCCTT	IDT	N/A
Primers/Probes for qPCR	IDT	See Table S2

(*Continued on next page*)

Continued

REAGENT or RESOURCE	SOURCE	IDENTIFIER
Software and algorithms		
Imaris	Bitplane	https://imaris.oxinst.com/
GraphPad Prism	GraphPad	https://www.graphpad.com/
CHOPCHOP	Labun et al.[59]	https://chopchop.cbu.uib.no/
AMT Imaging software V.7.0.1	Advanced Microscopy Techniques Corp.	https://www.amtimaging.com/
Spinnaker SDK software	FLIR	https://www.flir.com/products/spinnaker-sdk/
Fiji/ImageJ	Schindelin et al.[60]	https://fiji.sc/
Zen software	Zeiss	https://www.zeiss.com/microscopy/en/products/software/zeiss-zen.html
LabScribe ECG recording software	iWorx	https://iworx.com/labscribe/?v=7516fd43adaa
VisualSonics Echocardiogram Software	Fujifilm	VevoCQ
OpenCV	Open Source Computer Vision Library	https://opencv.org
scikit-learn	Scikit-learn	https://scikit-learn.org
pCLAMP 10	Moleculardevices	https://support.moleculardevices.com/s/article/Axon-pCLAMP-10-Electrophysiology-Data-Acquisition-Analysis-Software-Download-Page
Other		
High-speed camera	FLIR	BFS-U3-17S7M-C
Zebrafish ECG recording system	iWorx	ZS-200
Vevo2100 Imaging System	Fujifilm	Vevo2100
MX550S Ultrasound Transducer	Fujifilm	MX550S
Axopatch Amplifier	Moleculardevices	200B
PatchStar Micromanipulator	Scientifica	https://www.scientifica.uk.com/products/scientifica-patchstar-micromanipulator
Nikon Eclipse	Nikon	Ti
Axon Digidata	Moleculardevices	1550A

RESOURCE AVAILABILITY

Lead contact

Further information and requests for resources and reagents should be directed to the lead contact, Ankur Saxena (asaxena1@uab.edu).

Materials availability

All unique reagents generated in this study are available from the lead contact.

Data and code availability

- Data: Zebrafish heart proteomics mass spectrometry data have been deposited to the ProteomeXchange Consortium and are publicly available as of the date of publication. Accession numbers are listed in the key resources table.
- Code: This paper does not report original code.
- Any additional information required to reanalyze the data reported in this paper is available from the lead contact upon request.

EXPERIMENTAL MODEL AND STUDY PARTICIPANT DETAILS

Zebrafish model

Zebrafish husbandry

Zebrafish were treated and cared for according to the National Institutes of Health Guide for the Care and Use of Laboratory animals. All experiments were approved by the University of Illinois at Chicago Institutional Animal Care Committee. Zebrafish embryos were grown,

staged, and collected as previously described.[61,62] The transgenic zebrafish line *Tg(cmlc2:eGFP;gata1:dsRed)* was used in the AB wild-type background, and its abbreviation in the text is cmlc2:eGFP; gata1:dsRed.[56,57] For experiments using embryos, the sex was not determined, and therefore, sex distribution was random and roughly equal in all experimental groups and treatments. For experiments using adults, the sex was determined, and sex distribution was roughly equal in all experimental groups and treatments.

Generation of ttna$^{\Delta 9}$ in zebrafish and genotyping

The crRNA (AAGCTCAGTACGTTCTTCAC) was designed with the online bioinformatics tool CHOPCHOP[59] to direct Cas9 protein to the desired chromosomal location, (Chr9: 42905439–42905458, GRCz11), in *ttna*'s Ig-107 domain. TracrRNA, customized crRNA, and Cas9 protein were ordered from Integrated DNA Technologies (IDT). The injection solution containing assembled ribonucleoproteins was prepared according to an established protocol provided by IDT.[63] Briefly, the crRNA and tracrRNA were resuspended in Nuclease-Free IDTE Buffer (IDT) to final concentrations of 100 μM each. Then, 3 μL of crRNA, 3 μL of tracrRNA, and 94 of μL Nuclease-Free Duplex Buffer (IDT) were mixed and heated at 95°C for 5 min to create a 3 μM gRNA solution. The gRNA solution was cooled to room temperature on the bench top. 0.5 μL of 10 μg/μL Cas9 protein stock solution was added into 9.5 μL of Cas9 working buffer (20 mM HEPES; 150 mM KCl, pH 7.5) to get a 0.5 μg/μL working concentration. The injection solution containing the assembled RNP complexes was made by combining 3 μL of gRNA solution with 3 μL of Cas9 protein working solution and incubating at 37°C for 10 min. The solution was injected (0.7–1.5 nL) into wild-type AB strain zebrafish embryos at the one-cell stage. Genomic DNA were extracted with the Hot Sodium Hydroxide and Tris (HotSHOT) method: whole embryos or 3 mm tail-clip samples of adults were dissolved in 50 mM NaOH at 95°C for 15 min, cooled down, and neutralized with 1/10 NaOH volume of 1 M Tris-HCl, pH 8.0. DNA fragments for genotyping were amplified with DreamTaq Hot Start Green PCR Master Mix (Thermo Scientific, K9022) and primers (Forward: GCCTTCCTTCCACATTTATTTTCCA; reverse: CAGGCTATCAGTGCCCATCA) and then run on a 3% agarose gel. LA Taq DNA polymerase (TaKaRa, RR042B) was used to amplify DNA fragments for regular Sanger sequencing, performed by UIC's Genome Research Core.

Human induced pluripotent stem cell-derived atrial cardiomyocytes (hiPSC-aCM) model

Genomic editing of TTN in hiPSCs with CRISPR-Cas9

HiPSC lines were generated from patient's peripheral blood mononuclear cells (PBMCs) (IRB Protocol #2015-0681 "The Genetic Basis of Atrial Fibrillation"). The reprogramming process was completed with Sendai virus using the CytoTune-iPS 2.0 Sendai Reprogramming Kit (Thermo Fisher Scientific kit). After colony appearance at 3–4 weeks, colonies were manually picked. Generated hiPSC colonies were screened and karyotyped (Diagnostic Wicell Inc.). Our protocol typically yields ~80 to 90% pure iPSC-aCMs and <6% fibroblasts based on immunostaining analysis, as previously described[30,64] and shown in Figure S5.

The *TTN*-Δ9 CRISPR-Cas9 sgRNA (TGTTTCAGATGTTGCAATCA) and ssODN (CAATCATTGCACGCTTACTAATATCCTGGCCTT) were designed to target the wild-type (WT) genomic DNA location: chr2:178539785-178539811 (GRCh38.p13). *TTN*$^{+/+}$ hiPSCs were dissociated into single cells, then electroporated with Cas9 ribonucleoprotein (RNP) complexes targeting exon 352 and sgRNA using the Neon Transfection System (Invitrogen). Cells were transferred into one well of a Matrigel-coated 24-well plate containing 400 μL of mTesR with 10 mM Y-27632. After expansion for several days, half of the cell population was used to analyze editing efficiency with next-generation sequencing (NGS). Upon confirming editing efficiency, 96 individual cells were manually sorted to establish single-cell colonies. 50 edited clones were selected for expansion and verification by NGS sequencing. Karyotype analysis was performed by the Cytogenetics laboratory at WiCell Research Institute Inc. Twenty metaphase cells were harvested and their chromosomes were analyzed using the giemsa trypsin wright (GTW) banding method, showing a normal karyotype (46, XY).

HiPSC culture and atrial cardiomyocyte differentiation and maturation

To culture hiPSCs, the cells were seeded at an initial density of 500,000 cells/well on 6-well plates coated with human recombinant vitronectin (VTN). The hiPSCs were cultured in mTesR media with daily media exchanges until 80–90% confluent, after differentiation begins. After briefly washing hiPSCs with DPBS without Ca^{2+} or Mg^{2+}, Medium A (Day 1) of conditioned differentiation kit (Gibco) was added for 2 days. On Day 3, the media was replaced with Medium B of conditioned differentiation kit (Gibco) for 2 days. To guide hiPSC-CMs into atrial maturation, on Day 5, the cells were treated with 1 μM/all-trans retinoic acid (RA) for 4 days with media changes every 2 days.[65] Population purification was accomplished using glucose starvation and lactate replacement. Contracting monolayers were visualized between Days 9–12, depending on the cell culture and batch-batch variability.

Human atrial cardiac fibroblasts (aCFs) were purchased cryopreserved from Lonza and grown in medium containing 10% fetal bovine serum (FBS, Thermo Fisher Scientific) in Ham's F-12 medium containing L-glutamine (Gibco), 1% v/v penicillin/streptomycin (Corning), 4 ng/mL FGF-b (EMD Millpore), and human insulin (Sigma-Aldrich). aCFs were passaged by treatment with 0.05% trypsin/EDTA for 7 min, which was neutralized with medium containing serum. The cell suspension was then spun at 1100 rpm for 8 min to pellet the cells. The supernatant was removed, and cells were resuspended in fresh medium for further passaging or coculture experimentation. Cardiac fibroblasts were utilized between passages 3–6 to limit passage-passage variation. Prior to use in coculture studies, aCFs were growth arrested with 1 μg/mL mitomycin C (Millipore Sigma).

In order to improve maturity and control homotypic vs. heterotypic interactions, hiPSC-aCMs and aCFs were sequentially seeded onto patterned plates to create micropatterned cocultures. Briefly, an SU-8 mold was fabricated with 80 μm pillars and 55 μm trenches. To create

polydimethylsiloxane (PDMS, Dow-Corning) stamps, Sylgard-184 base and curing agents were mixed at a 10:1 ratio (w/w) and subsequently cast onto SU-8 molds, degassed, and thermally cured at 75°C for 1 h. To create micropatterns for cell seeding, tissue culture polystyrene (TCPS) plates were exposed to oxygen plasma for 2 min and then treated with 5% (3-Aminopropyl)triethoxysilane (APTES, Sigma-Aldrich) in 95% ethanol for 30 min in order to improve adhesion of the PDMS stamp to the plate. The plates were then dried and cured at 80°C for 1 h. PDMS stamps were placed in each well, followed by exposure to oxygen plasma to etch the APTES unprotected by the PDMS stamp in order to improve pattern distinction. Next, 0.05% bovine serum albumin (BSA, Fisher Scientific) dissolved in ddH2O (w/v) was added to the microchannels created between the plate and PDMS stamp via vacuum suction. The BSA treated plates were incubated overnight at 4°C, rinsed with ddH2O to remove excess BSA, dried, and sterilized via UV treatment. Finally, 30 μg/mL fibronectin (EMD Millpore) in 1x DPBS without calcium and magnesium was added to the BSA-blocked plates and incubated overnight at 4°C. Prior to cell seeding, the plates were rinsed with 1x DPBS without calcium and magnesium.

On Day 15, we dissociated the hiPSC-aCMs into single cells and reseeded onto fibronectin (FBN) coated micropatterned plates at a density of 800,000 cells/mL. To dissociate hiPSC-aCMs, media was aspirated and the cells were incubated with DPBS without calcium or magnesium for 20 min in 37°C, followed by 5 min in TrypLE in 37°C and 20 min in 25 μg/mL of liberase at 37°C. The cells were dissociated with gentle aspiration, centrifuged for 5 min at 500 g, then resuspended in Cardiomyocyte Maintenance Media (CMM; Gibco) supplemented with 10% FBS. Plates were gently shaken every 20 min for 3 h to ensure attachment to patterns. The following day, the media was changed to CMM with 5% FBS. The next day, atrial fibroblasts were seeded (200,000 cells/well in a 12-well plate). Two hours prior to fibroblast seeding, a half media change was performed with media containing 50 μg/mL collagen (to a final concentration of 25 μg/mL). Then the media was removed and replaced with electrometabolic maturation (EMM) media, after which the EMM protocol was applied.[35]

Magnetic cell sorting

After dissociating hiPSC-aCMs as described above, cells were centrifuged at 500 g for 5 min. After removing the supernatant, cells were resuspended in 80 μL of MACS buffer (Miltenyi Biotec) per 500,000 cells. 20 μL Non-Cardiomyocyte Depletion Cocktail (Miltenyi Biotec) was added per 500,000 cells, followed by gentle mixing and incubation for 5 min at 4°C. The cells were then washed in 1 mL of MACS buffer, followed by centrifugation at 200*g* for 5 min. The cells were resuspended in 80 μL of MACS buffer, mixed with 20 μL of Anti-Biotin Microbeads (Miltenyi Biotec), and incubated for 10 min at 4°C. The cell volume was increased to 500 μL. An LS column was hydrated in the MidiMACS Separator (Miltenyi Biotec) with 3 mL of MACS buffer, and the 500 μL cell sample was passed through. The column was washed with 3x3 mL of MACS buffer. All flow through is centrifuged at 200 g for 5 min. The cell pellet is resuspended in CMM supplemented with 10% FBS and penicillin/streptomycin, then seeded onto fibronectin-coated plates at a density of 500,000–750,000 cells/mL. Cell sorting was performed prior to immunofluorescence, RT-PCR, RNA-sequencing, high-throughput electrophysiology (SyncroPatch), western blotting, and co-immunoprecipitation experiments to ensure all analysis was performed on a purely atrial cardiomyocyte population.

METHOD DETAILS

In situ hybridization chain reaction (HCR)

Zebrafish embryos were fixed at 48 hpf and the HCR v3.0 protocol was used as previously described[66,67] with custom-designed probe sets targeting zebrafish *ttna*$^{\Delta 9}$ deleted region or the 1500-base-pair sequence flanking the deleted region (Molecular Instruments, Inc.). Embryos were also stained with DAPI (1:2000) to label nuclei. 2 pmol of each HCR probe set was hybridized at 37°C overnight in hybridization buffer, followed by washes at 37°C. Probes were detected by annealing of fluorescent hairpins in amplification buffer overnight at room temperature, followed by washes with 5x SSC/0.1% Tween 20. HCR probe sets, fluorescent hairpins, and buffers were purchased from Molecular Instruments, Inc.

Zebrafish transmission electron microscopy

Zebrafish embryos were anesthetized at 48 hpf with tricaine, and zebrafish adults were euthanized by rapid chilling in ice water bath. Adult zebrafish hearts were dissected out as previously described,[68] and atria and ventricles were then separated. Whole embryos and dissected adult atria and ventricles were fixed in 2% PFA and 2.5% glutaraldehyde in 0.1 M Sodium Phosphate Buffer, pH 7.4 for 2 h at room temperature, and then overnight at 4°C. Fixed samples were then washed in 0.1 M Sorensen's sodium phosphate buffer (SPB, pH 7.2) and post-fixed in buffered 1% osmium tetroxide for 1.5 h. After further buffer washes, samples were dehydrated in ascending concentrations of ethanol leading to 100% ethanol, followed by 2 changes in propylene oxide (PO) transition fluid. Specimens were infiltrated overnight in a 1:1 mixture of PO and LX-112 epoxy resin and for a minimum of 3 h in 100% pure LX-112 resin, then placed in a 60°C oven to polymerize for 3 days. Alternatively, embryonic specimens were embedded in LX-112 resin between 2 sheets of thin Aclar plastic. Semi-thin sections (1.0 μm) were cut and stained with 1% Toluidine blue-O to confirm orientations and/or areas of interest. Ultra-thin sections (70–80 nm) were cut using a Leica Ultracut UCT model ultramicrotome, collected onto 200-mesh copper grids, and contrasted with 6% uranyl acetate and lead citrate stains. Specimens were examined using a JEOL JEM-1400 Flash transmission electron microscope operating at 80 kV. Micrographs were acquired using an AMT Side-Mount Nano Sprint Model 1200S-B and/or BioSprint 12M-B cameras, loaded with AMT Imaging software V.7.0.1.

Zebrafish adult survival determination

Embryos from three *ttna*$^{\Delta 9/+}$ incrosses were genotyped at 1 dpf, and 23.3% of them were *ttna*$^{\Delta 9/\Delta 9}$. Adults from 4 *ttna*$^{\Delta 9/+}$ incrosses were genotyped at 6–8 months age; 18.3% were *ttna*$^{\Delta 9/\Delta 9}$.

Zebrafish live imaging and cardiac parameter measurements

48, 72, and 96 hpf cmlc2:eGFP; gata1:dsRed-dual positive embryos were embedded in 0.9% low-melting agarose and covered with Danieau solution. Lateral view videos of whole embryos were recorded with Spinnaker SDK software (FLIR) and a high-speed camera (BFS-U3-17S7M-C, FLIR) through Axio Zoom.V16 microscope (ZEISS) at room temperature with the following frame rates: heart contraction, 50 frame per second (fps); blood circulation, 195–202 fps). Heart rate and rhythm were measured and analyzed based on an established method, ZebraPace.[69] Fiji/ImageJ[60] was used to measure the following parameters: wall thickness of atria and ventricles, area of blood pooling, area of atria and ventricles at the end-diastolic (EDA) and end-systolic (ESA) phases, and ventricular long diameters (D_L) and short diameters (D_S) at ED and ES. Fractional area change (FAC), end-diastolic volume (EDV), end-systolic volume (ESV), ejection fraction (EF), and red blood cell (RBC) velocity in the dorsal aorta were calculated by the following equations, which have been previously described[70]:

$$\text{FAC (\%)} = \frac{EDA - ESA}{EDA} \times 100$$

$$\text{Volume} = \frac{1}{6} \times \pi \times D_L \times D_S^2$$

$$\text{EF (\%)} = \frac{EDV - ESV}{EDV} \times 100$$

$$\text{RBC velocity} = \frac{\sqrt{(x_2 - x_1)^2 - (y_2 - y_1)^2}}{\Delta t}$$

The retrograde flow fraction was measured as previously described.[71] Briefly, the movement of gata1:dsRed-labeled blood cells was captured using the same high-speed camera, and the blood flow direction during each cardiac cycle was determined for every frame. The retrograde flow fraction (RFF) was calculated by dividing the total number of frames showing retrograde flow from the atrium to the inflow tract by the total number of frames per cardiac cycle.

Zebrafish embryo quantitative reverse transcription PCR (RT-qPCR): Total RNA from dechorionated zebrafish embryos at 48 or 96 hpf was extracted with RNeasy Mini Kit (QIAGEN). cDNA was synthesized using SuperScript IV VILO Master Mix (Invitrogen). qPCR was performed with KiCqStart SYBR Green qPCR ReadyMix (Sigma) or iTaq Universal SYBR Green Supermix (Bio-Rad) and CFX Connect Real-Time PCR Detection System (Bio-Rad). Each genotype contained 3 biological replicates, and each biological replicate contained 4–5 embryos. mRNA expression levels of target genes were normalized to the expression of *rpl13*. Primers used for RT-qPCR of *nppa*, *nppb*, *neurod1*, *kcnq1*, *kcne1*, and *rpl13* are listed in Table S2.

Zebrafish adult heart dissection and histology

Adult zebrafish were euthanized by rapid chilling in an ice water bath, and hearts and surrounding tissue were dissected out and fixed in 4% paraformaldehyde (PFA) phosphate-buffered saline solution for 1.5 h at room temperature and then 24 h at 4°C. Following the fixation, zebrafish specimens were loaded into ASP 300s automated tissue processor (Leica Biosystems) and dehydrated by a series of ascending graded ethanol, cleared in xylene, and infused with paraffin following a preset protocol. Samples were then embedded in paraffin in lateral orientation, and 5 μm sections were cut and mounted on positively charged slides, dried, and baked at 60°C for 1 h. Adhered sections were deparaffinized in Leica Autostainer XL automated stainer (Leica Biosystems) using xylene and descending ethanol series, rehydrated in tap water, and stained with hematoxylin (Vintage Hematoxylin, StatLab#SL100) and eosin (Vintage Eosin, StatLab #SL101) using a preset protocol. A subset of slides was also stained with modified Masson's trichrome stain. In brief, deparaffinized sections were incubated in Bouin's fixative (Electron Microscopy Sciences, #26367-01) for 1 h at 56°C, rinsed with tap water, stained with Biebrich Scarlet Acid Fuchsin solution (Electron Microscopy Sciences, #26033-25) for 8 min at room temperature, washed in distilled water, incubated in Phostotungsten/Phosphomolybdic Acid (StatLab, #AHP0543) for 15 min, and stained with Aniline Blue solution for 4 min. Both H&E and Trichrome-stained slides were dehydrated on Autostainer XL and mounted with Micromount media (Leica Biosystems) on CV5030 automated coverslipper (Leica Biosystems).

Adult heart size measurement

Dissected whole hearts were imaged with a brightfield microscope and Zen software (Zeiss). Atrial and ventricular sizes were quantified with ImageJ and normalized to the standard length (distance from the snout to the caudal peduncle) of each zebrafish.

Zebrafish adult echocardiography

Adult zebrafish (14–15 months old) were anesthetized for 3 min in a chamber containing system water and 0.2 mg/mL tricaine, after which echocardiography was performed using the Vevo2100 Imaging System and VisualSonics Software equipped with the MX550S transducer (bandwidth 25–55 MHz, central operating frequency 40 MHz) with continued anesthesia. Two-dimensional (B-mode) images were obtained in the long axis and short axis views along with color Doppler and pulsed wave Doppler imaging, as previously described.[72] We optimized B-mode imaging quality by adjusting focal depth, gain, and image width/depth, with ventricular inflow measured just distal to the atrioventricular valve leaflet

tips by pulse wave Doppler imaging after ensuring parallel beam direction to flow. The heart rate was averaged from 5 s windows with the B mode and Doppler measurements averaged across at least 3 cardiac cycles. We indexed measurements by body surface area, which was calculated using previously validated methods.[73] Zebrafish were subsequently transferred to system water without anesthetic and monitored for recovery.

Zebrafish adult electrocardiography (ECG)

Adult zebrafish ECG recording was performed as previously described[74] with iWorx ZS-200 zebrafish ECG recording system. Briefly, 6–11 months old zebrafish were anesthetized in 200 mg/L Tricaine solution for 7–8 min until there was no gill motion. Each anesthetized zebrafish was transferred to the ECG chamber and positioned on its back, with electrodes placed on the chest and along the midline. ECG was recorded for at least 2 min at 27°C–28°C and analyzed with iWorx LabScribe ECG recording software (zebrafish default setting). After recording, each zebrafish was transferred to regular system water for recovery. Statistical analysis of AF incidence was performed with Fisher's exact test.

Zebrafish proteomics analysis

Adult zebrafish were euthanized by rapid chilling in an ice water bath, and hearts were dissected as previously described.[68] Atria and ventricles were then separated, and 10 atria or 10 ventricles were pooled for each genotype and processed as previously described.[75] Briefly, pooled samples were homogenized in buffer (50 mM Tris-HCl, pH 8.5, 5 mM EDTA, 150 mM NaCl, 10 mM KCl, 1% Triton X-100, protease inhibitor (SKU#11836170001, Roche)) and centrifuged at 15,000 g for 20 min at 4°C to collect the soluble supernatant. Protein was precipitated with ice-cold acetone (25% final concentration) for 1 h at −20°C, and the pellet was collected after centrifugation at 400*g* for 1.5 min and dissolved in 8 M urea, 100mM Tris-HCl, pH 8.5. Protein sample was reduced by 5 mM Tris(2-carboxyethyl)phosphine (TCEP) at room temperature for 15 min, followed by 50 mM chloroacetamide (CAA) alkylation in the dark at room temperature for 20 min. Protein was digested with trypsin (Promega, V5111) at 1:50 (w/w) ratio for 20 h at 37°C. Digestion was quenched by formic acid and the supernatant was collected after centrifugation at 18,000 g for 20 min at 4°C. Digestion product was desalted with C18 column (Pierce Peptide Desalting Spin Column) according to the manufacturer's protocol. Peptide sample was cleaned with detergent removal column (Pierce). 2 μg peptide from each replicate sample was isobaric labeled with TMT6plex and fractionated with High pH Reversed-Phase Peptide Fractionation Kit (Pierce). Fractions were dried by SpeedVac, reconstituted in 0.1% formic acid, and analyzed by an Ultimate 3000 RSLCNano UPLC system coupled to a Thermo QExactive HF quadrupole−Orbitrap mass spectrometer. The HPLC was equipped with fused-silica capillary analytical columns (Acclaim PepMap, 75 μm * 25 cm, 3 μm, 100 Å). A stepped 90 min gradient of 80% acetonitrile (solvent B) and 0.1% formic acid (solvent A) at 300 nL/min flow rate was used: 5%–60% B in 70 min, 60%–95% B in 5 min, and 95% B for 15 min. The survey scan range was from 375 to 1600 m/z at a resolution of 120,000 with AGC target of $3*10^6$. The top 10 intense peaks were selected with 1.2 m/z isolation window for MS/MS at resolution of 60,000 with AGC target of 10^5. MS/MS was performed with fixed first mass of 100.0 m/z. 32% normalized collision energy (NCE) was applied for peptide fragmentation. LC/MS/MS raw files were searched using MSFragger[76] and the Uniprot zebrafish database (July 2021 release) with these parameters: full tryptic specificity, miss cleavage site maximum 2, carbamidomethylation of cysteine residues and TMT6plex (K) as fixed modification; protein N terminal acetylation, TMT6plex (peptide N-term), and methionine oxidation as variable modifications. False discovery rate for protein were set to 1%. The mass spectrometry proteomics data have been deposited to the ProteomeXchange Consortium via the PRIDE[77] partner repository with dataset identifier PXD038300.

Electrophysiological recording of zebrafish atrial cardiomyocytes

Adult zebrafish atrial cardiomyocytes were isolated as previously described[78] at 12 months old. Briefly, atria and ventricles from 3 to 4 zebrafish hearts were separated under a microscope, and each tissue type was pooled together in tricaine solution (Sigma, cat. no. A5040), followed by transfer to a microcentrifuge tube containing 1 mL perfusion buffer (10 mM HEPES, 30 mM taurine, 5.5 M glucose, and 10 mM BDM in 1x PBS). The combined tissue strips were then transferred to a microcentrifuge containing 750 μL digestion buffer (5 mg/mL Collagenase II and Collagenase IV and 12.5 μM $CaCl_2$ in perfusion buffer). Tissue strips were gently agitated every 10 min for 1–2 h. At the end of digestion, an equal volume of stop buffer (10% FBS and 12.5 μM $CaCl_2$ in perfusion buffer) was added, the suspension was centrifuged at 500 g, the pellet was washed and centrifuged with a series of calcium reintroduction buffers (5% FBS +12.5 μM, 62 μM, 112 μM, 212 μM, 500 μM, and 100 μM $CaCl_2$ in perfusion buffer), and the final cell pellet was resuspended in the respective external solution to use for AP recordings. APs were recorded using the amphotericin-B patch clamp method, as described previously.[79,80] Briefly, isolated atrial myocytes were bathed with a modified Tyrode's solution containing (mM): 140 NaCl, 5.4 KCl, 1.8 $CaCl_2$, 1.0 $MgCl_2$, 5 glucose, 5 HEPES; pH 7.4 (NaOH). Patch pipette resistance was within 7–10 MΩ when filled with intracellular solution containing (mM): 125 K-gluconate, 20 KCl, 10 NaCl, 0.44 amphotericin-B, 10 HEPES; pH 7.2 (KOH). Action potentials were elicited by 5 ms sub-threshold current steps through the patch pipette. Axopatch 200B amplifier and Digidata 1550A were used for data acquisition, and analysis was performed using pClamp 9.0 software. Action potential duration (APD) was measured as the duration to three different percentages of repolarization: APD_{20}, APD_{50}, APD_{90}.

Zebrafish morpholino treatment

nppa translation-inhibiting morpholino (TCAGAATTAGTCCCCCGGCCATCTC), *nppb* translation-inhibiting morpholino (TGTGAAGCGATTTCATGTCTCCTGA) or negative control morpholino (CCTCTTACCTCAGTTACAATTTATA) was diluted in water and injected into embryos at one-cell stage with concentration of 2 ng per embryo. The specificity of morpholino targeting *nppa* was tested in a previous study.[58]

Zebrafish embryo drug treatment

Dechorionated cmlc2:eGFP-positive zebrafish embryos' atrial contraction was measured at 48 hpf, as described above. Embryos were then individually transferred into Danieau solution containing either 1% DMSO for control groups or 10 μM HMR-1556 (Sigma-Aldrich) in 1% DMSO for experimental groups. After 4 h of treatment, atrial contraction for each embryo was remeasured.

Immunofluorescence cellular preparation, imaging, and analysis

hiPSC-aCMs were dissociated using the above protocol and replated onto confocal grade polymer bottom dishes (ibidi), then allowed to recover for 2 days. The cells were washed with PBS, fixed with 4% paraformaldehyde (PFA) in 37°C for 10 min, permeabilized using 0.1% Triton X-100 for 15 min, and blocked with 3% BSA for 1 h. Primary antibody was diluted 1:200 in 0.1% BSA and incubated in 0.1% BSA in 4°C overnight. Primary antibodies used were cTnT (Abcam; ab45932) and α-actinin (Abcam; EA-53 ab9465). Secondary antibody was incubated at a 1:500 dilution in 0.1% BSA for 1 h. Nuclei were stained with DAPI at 1:1000 dilution in PBS for 20 min. The cells were visualized using Zeiss Laser Scanning Confocal Microscope (LSM 710) (META) with a 63x oil objective and analyzed with ImageJ. Sarcomere length was determined by measuring the distance between long axis intensity peaks indicating cellular sarcomeric striations (stained with α-actinin). Ten sarcomere lengths were obtained per cell. In order to quantify disorganization of sarcomeres, α-actinin objects were segmented with Trainable Weka Segmentation[81] in ImageJ, skeletonized, and converted into datasets of branches. Branch angles for each cell were adjusted by the cell's long-axis. The number of branches angled 15° within 0° or 90° were counted and divided by the total number of branches. Kernel density was used to estimate angular distributions.

Transmission electron microscopy (TEM) sample preparation

hiPSC-aCMs are washed in wells with DPBS without Ca^{2+} and Mg^{2+} to remove protein deposition. Warmed (37°C) 2.5% glutaraldehyde in 0.1 M Sorenson's Buffer was added for 60 min at room temperature for the first round of fixation, followed by gently scraping cells into a microcentrifuge tube prefilled with 2.5% glutaraldehyde in 0.1 M Sorenson's buffer. Samples were centrifuged at 2500 g for 10 min at room temperature, and the pellet was dislodged and flipped with a hypodermic needle to ensure fixative solution penetrated the entire sample. The pellet was kept at room temperature to fix for an additional 60 min, then the 2.5% glutaraldehyde in 0.1 M Sorenson's buffer solution was removed and replaced with 1% glutaraldehyde +4% paraformaldehyde in 0.1 M Sorenson's buffer and stored at 4°C.

Contractility analysis

Dense optical flow with the Gunnar-Farneback algorithm[82] was applied to brightfield monolayer contraction videos in OpenCV using python. The magnitude of every vector per frame was summed, divided by the area of the active field, and plotted in waveform charts. To expand features for classification, the net vector from the field was summed and integrated. The feature list included 3 consecutives past timepoints and 1 future timepoint with a univariate Gaussian filter applied to velocities. A random forest classifier[83] from sklearn.ensemble[84] was trained with segments of annotated waveform charts resulting in a 97.7% validation accuracy. The classifier was applied to all waveform data for subsequent data tabulation.

HiPSC-aCMs RNA isolation, cDNA synthesis, and RT-qPCR: TRIzol (Invitrogen) was used to extract total RNA from hiPSC-aCMs, which was then reverse-transcribed using SuperScript III Reverse Transcriptase (ThermoFisher) according to manufacturer protocols. RT-qPCR TaqMan Fast Advanced Master Mix (ThermoFisher) was used for RT-qPCR. Glyceraldehyde 3-phosphate dehydrogenase (GAPDH) was used to normalize mRNA expression, and data was analyzed with the ΔΔCt method. TaqMan probes for *KCNQ1*, *KCNE1*, GAPDH, and primers for *NPPA* were listed in Table S2.

Myocyte isolation for automated electrophysiology

Myocytes grown in 6-well plates were isolated using the following protocol: Media was aspirated from wells, 1 mL PBS without Ca/Mg was added to each well and swirled gently 2–3 times, and then was replaced with 2 mL fresh PBS without Ca/Mg per well and incubated for 30 min at 37°C, 5% CO2. Solution was then removed, and 1 mL PBS without Ca/Mg + Liberase (25 μg/mL. Liberase TH Research Grade, Roche) was added to each well. Cells were incubated for 25 min at 37°C, 5% CO2. After the incubation, cells in each well were separated by gentle trituration using a 5 mL pipette and cell mixture transferred to a 15 mL conical tube. 1 mL of PBS without Ca/Mg was added to each well to recover remaining cells and added to the conical tube. Cells were gently mixed by aspirating up and down with 5 mL pipette. An aliquot (500 μL) was used to determine cell number and viability with automated cell counting (ViCell, Beckman Coulter). Cells were diluted to 500,000 cells/mL with PBS without Ca/Mg and allowed to recover 20–30 min at 15°C while shaking on a rotating platform at 250 rpm before starting recordings.

Automated electrophysiology

We performed automated patch clamp recording using the SyncroPatch 384i platform (Nanion Technologies) using single-hole, 384-well thin-glass recording chips. To record sodium current (I_{Na}) and calcium current (I_{Ca}), the internal solution contained (in mM): CsF 110, CsCl 10, NaCl 10, HEPES 10, EGTA 20, ATP-Mg 4, with the final pH adjusted to 7.2 with NaOH. The standard external solution contained (in mM): NaCl 140, KCl 4, $CaCl_2$ 2, $MgCl_2$ 1, HEPES 10, glucose 5. I_{Ca} was also recorded after diluting the standard external solution 1:1 with a Ba^{2+}-containing, Ca/Mg-free external solution (in mM): NaCl 140, KCl 4, HEPES 10, glucose 5, $BaCl_2$ 30, with the final pH adjusted to 7.4 with NaOH. I_K was

recorded using an internal solution containing (in mM): KF 60, KCl 60, NaCl 10, HEPES 10, EGTA 20, ATP-Mg 2, with the final pH adjusted to 7.2 with KOH. The external solution contained (in mM): NaCl 140, KCl 4, $CaCl_2$ 2, $MgCl_2$ 1, HEPES 10, glucose 5, with the final pH adjusted to 7.4 with NaOH. Non-specific currents were removed by recording whole-cell currents following the addition of 1 μM HMR-1556 or 2 μM JNJ-303 (Tocris) and digital subtraction from control currents. Only blocker-sensitive currents were analyzed.

Pulse generation and data collection were conducted with PatchController384 V.1.9.7 software (Nanion Technologies). Whole-cell currents were recorded at room temperature in the whole-cell configuration, filtered at 3 kHz and acquired at 10 kHz for I_{Na} and I_{Ca} and filtered at 3 kHz and acquired at 1 kHz for I_K. The access resistance and apparent membrane capacitance were estimated using built-in protocols. Access resistance compensation was set to 80% and leak and capacitance artifacts were subtracted out using the P/4 method.

Voltage protocols: I_{Na}: Peak whole-cell currents were elicited from a holding potential of −120 mV using 500 ms depolarizing pulses (from −120 + 60 mV in +10mV steps, every 7.5 s), followed by a 20 ms step to −20 mV where currents were measured to determine voltage-dependence of inactivation. I_{Ca}: Whole-cell currents were measured from a holding potential of −120 mV. I_{Na} was inactivated by a 2000 ms pulse at −80mV, preceded by 800 ms ramp pulse to −50 mV before each test pulse. I_{Ca} was then elicited by 500 ms pulses from −80 to +50 mV in +10mV steps, every 10 s). I_{Ks}: Whole-cell currents were elicited from a holding potential of −80 mV using 2000 ms depolarizing pulses (from −60 mV to +60 mV in +10mV steps, every 15 s), followed by a 2000 ms step to −30 mV. Peak currents were measured 1990 ms after the start of the depolarizing voltage pulse.

Data analysis for automated electrophysiology

Data were analyzed and plotted using a combination of DataController384 V1.8.0.24 (Nanion Technologies, Excel (Microsoft Office 365, Microsoft), SigmaPlot V14 (Systat Software, Inc., San Jose, CA) and GraphPad Prism V9.31 (GraphPad Software, San Diego, CA). Additional custom semi-automated data handling routines were used for rapid analysis of current density and voltage-dependence of activation and inactivation. Whole-cell currents were normalized for membrane capacitance and results expressed as mean ± SEM. I_{Na} voltage dependence of activation and inactivation: Whole-cell conductance (G_{Na}) was calculated as $G_{Na} = I/(V - E_{rev})$, where I is the measured peak current, V is the step potential, and E_{rev} is the calculated sodium reversal potential. G_{Na} at each voltage step was normalized to the maximum conductance between −120 mV and 40 mV. To calculate voltage dependence of activation, normalized G_{Na} was plotted against voltage and fitted with the Boltzmann function. Voltage dependence of inactivation was determined by plotting the normalized currents measured at the −20 mV step against the first voltage step voltages from −120 to 0 mV and fitted with the Boltzmann function.

Optical voltage mapping and drug exposures

Cells were washed 5 times with indicator-free Tyrode's solution. After reconstituting the 2 mM VF2.1Cl dye to 1 mM in 10% Pluronic-F127, then diluting the dye to 100 nM in Tyrode's solution, the VF2.1Cl dye was added to each well for 50 min in a 37°C 5% CO_2 incubator. The cells were then washed 5 times with indicator-free Tyrode's solution and returned to the 37°C, 5% CO_2 incubator for 10 min to recover. The dye was excited at 514 nm wavelength, and time series images were acquired at an acquisition frequency of 45 Hz for 40 s in Epi-fluorescence mode using Zeiss Laser TIRF Microscope fitted with a Hamamatsu ORCA-Flash 4.0 V3 digital CMOS camera C13440-20CU. For drug challenges, dofetilide (3 nM), HMR-1556 (1 μM), and verapamil (1 μM) were added 30 min prior to image acquisition and incubated in a 37°C, 5% CO_2 incubator. APD_{90} was calculated as described previously.[85]

QUANTIFICATION AND STATISTICAL ANALYSIS

Unless otherwise noted, data are presented as mean ±95% confidence interval. For data with normal distribution, parametric unpaired and two-tailed T-test was used to determine statistical significance between two groups, and either one-way or two-way ANOVA for multiple groups with post-hoc Bonferroni corrections. For data with nonnormal distribution, nonparametric Mann-Whitney *U* test was used. All statistical analyses for significance were performed using Microsoft Excel or GraphPad Prism 9.2. ns $p > 0.05$; * $p < 0.05$; ** $p < 0.01$; *** $p < 0.001$; ****$p < 0.0001$.